

Supervisor: Assoc. Prof. Kamen Asenov Kozarev
Sofia March 29, 2024

Mohamed Elsayed Nedal AbuLainaim Mohamed

4.1 Physics, Specialization: Heliophysics
Author of PhD dissertation

Solar Transients From The Sun to Earth Coronal Bright Fronts, Radio Bursts, and Energetic Protons

Institute of Astronomy and National Astronomical Observatory



Bulgarian Academy of Sciences



Acknowledgments

Pursuing a doctoral degree during a global pandemic has been a challenging yet incredible and rewarding journey of personal growth and intellectual stimulation. This dissertation would not have been possible without the guidance and support of many incredible people around me.

First and foremost, I am deeply grateful to my advisor, Dr. Kamen Kozarev. Thank you for giving me the opportunity to work on such an interesting and exciting project (SPREADFAST: Solar Particle Radiation Environment Analysis and Forecasting—Acceleration and Scattering Transport). Thank you for granting me the flexibility to work and the freedom to explore and experiment with new ideas. Your insightful feedback, unwavering encouragement, and dedication to my success have been invaluable throughout this process. I am incredibly grateful for your patience during moments of doubt and your enthusiasm that reignited my passion when I needed it most, as well as your ability to help me refine my thoughts and ideas. I am truly fortunate to have had you as my advisor.

I extend my heartfelt gratitude to my colleagues in the Sun and Solar System Department at the Institute of Astronomy and National Astronomical Observatory, Bulgarian Academy of Sciences: Dr. Rositsa Miteva, Dr. Oleg Stepanyuk, and Dr. Momchil Dechev. Thank you for the stimulating discussions, the collaborative spirit, and for generously sharing your expertise. Your valuable advice, feedback, and support have greatly enriched my experience. I am also grateful to Nestor Arsenov and Yordan Darakchiev for the insightful discussions on deep learning models, which have been valuable in shaping my understanding.

A special thank you goes to Dr. Pietro Zucca and Dr. Peijin Zhang for introducing me to the fascinating world of radio observations from the Low-Frequency Array (LOFAR) and guiding me through the intricacies of working with the data and relevant software. Thank you for the cherished moments we shared during my visits to the Netherlands and other places; those experiences have left an indelible imprint.

Furthermore, I am grateful for the financial support provided by the MOSAICS project (Modeling and Observational Integrated Investigations of Coronal Solar Eruptions) and the STELLAR project (Scientific and Technological Excellence by Leveraging LOFAR Advancements in Radio Astronomy). This funding has been a tremendous blessing, allowing me to focus wholeheartedly on my research without financial constraints, and has significantly contributed to the successful completion of this dissertation.

My deepest appreciation goes to my family. Thank you for your unwavering love, belief in me, and constant prayers and encouragement throughout this long journey. You have been my source of strength and motivation. To my dear friends, thank you for the countless moments of laughter, the much-needed distractions, and for reminding me of the vibrant world beyond academia. Your support and companionship, especially during my initial period in Bulgaria, have rendered this experience all the more enjoyable.

Finally, I would like to acknowledge and express my heartfelt gratitude to all those who have directly or indirectly contributed to this work. The collective efforts of all contributors, no matter how big or small, have played a crucial role in bringing me to this point and the successful completion of this dissertation. Those four years were the most beautiful time of my life and I will always cherish them. Thank you all from the bottom of my heart.

This interdisciplinary thesis advances our understanding of solar transients by investigating the early dynamics of Coronal Bright Fronts (CBFs), diagnosing solar type III radio bursts, and forecasting Solar Energetic Particle (SEPs). Integrating these studies, we reveal the relationships among these phenomena and their implications for space weather forecasting. Our analysis of 26 CBFs, using Solar Particle Emission Analysis and Forecasting—Acceleration and Scattering Transport (SPEDFAST) framework and data from the Atmospheric Imaging Assembly (AIA) and the Large Angle and Spectrometric Coronagraph (LASCO) instruments, unveils temporal evolution, plasma properties, and comprehensive characteristics. The second study, employing the Low-Frequency Array (LOFAR) and Parker Solar Probe (PSP), characterizes 9 type III radio bursts in the frequency, plasma properties, and comprehensive characteristics. The Low-Frequency Array (LOFAR) and Parker Solar Probe (PSP) instruments, unveils temporal evolution, plasma properties, and comprehensive characteristics. The second study, employing the Low-Frequency Array (LOFAR) and Parker Solar Probe (PSP), characterizes 9 type III radio bursts in the frequency, plasma properties, and comprehensive characteristics. The second study, employing the Low-Frequency Array (LOFAR) and Parker Solar Probe (PSP), characterizes 9 type III radio bursts in the frequency, plasma properties, and comprehensive characteristics. The second study, employing the Low-Frequency Array (LOFAR) and Parker Solar Probe (PSP), characterizes 9 type III radio bursts in the frequency, plasma properties, and comprehensive characteristics. The second study, employing the Low-Frequency Array (LOFAR) and Parker Solar Probe (PSP), characterizes 9 type III radio bursts in the frequency, plasma properties, and comprehensive characteristics.

Abstract

Supervisor: Assoc. Prof. Kamen A. Kozarev

Sun and Solar System Department
Bulgarian Academy of Sciences

Institute of Astronomy and National Astronomical Observatory

Mohamed Elsayed Nedal AbuAlamain Mohamed

and Energetic Protons

Coronal Bright Fronts, Radio Bursts,

Solar Transients From the Sun to Earth

Zhu, H., Zhu, W., & He, M., 2022, Solar Physics, 297, 157

Zhang, W., Zhao, X., Feng, X., et al. 2022a, The Astrophysical Journal, 932, 17

Zhang, P., Zucca, P., Kozarev, K., et al. 2022b, The Astrophysical Journal, 932, 17

Zhang, P., Wang, C., Bi, & Yu, D., 2018, *Astrophysics & Space Physics*, 618, A165

Zhang, J., Deere, K., & Webb, D., et al. 2007, *Journal of Geophysical Research: Space Physics*, 112

Zhang, J., Cheung, X., & Ding, M.-d., 2012, *Nature communications*, 3, 747

Zhang, J., Peter, H., et al. 2018, *Space Science Reviews*, 214, 1

Xie, H., Ouman, L., & Lawrence, G., 2004, *Journal of Geophysical Research: Space Physics*, 109

Xapatos, M. A., Stauffer, C. A., Jordan, T. M., Adams, J. H., & Dietrich, W. F., 2012, *IEEE Transactions on Nuclear Science*, 59, 1054

Contents

1	Introduction	2
1.1	Background and Motivation	2
1.1.1	Coronal Waves	3
1.1.2	Solar Radio Bursts	4
1.1.3	Solar Energetic Protons Forecasting	5
1.2	Objectives and Scope	5
1.3	Outlines	6
2	Remote Observations: Early-stages and Later-stages of Eruption	7
2.1	Introduction	7
2.2	EUV Observations	8
2.3	Data Analysis and Methods	10
2.4	CBF Kinematics and Geometric Modeling: Case Study May 11, 2011	10
2.4.1	Event Context	10
2.4.2	Low Corona Part	11
2.4.3	Middle/Outer Corona Part	11
2.5	Statistical Study	11
2.6	Conclusions	18
3	Solar Radio Observations: Integrating Data for Coronal Diagnostics	19
3.1	Introduction	19
3.2	Observations	19
3.2.1	PSP Observations	22
3.2.2	LOFAR Observations	22
3.3	Methods	22
3.3.1	Imaging of Radio Sources	22
3.3.2	Modeling	24
3.4	Results and discussion	24
3.4.1	Type III Radio Burst Detection and Characterization	24
3.4.2	Imaging of Radio Emission Sources	24
3.4.3	Plasma Diagnostics and Magnetic Field Analysis	26
3.5	Summary and conclusions	26
4	Modeling and Forecasting of Solar Energetic Protons	30
4.1	Introduction	30
4.2	Solar Proton Flux Forecasting with Deep Learning Models	30
4.2.1	Data Preparation	30
4.2.2	Method	31
4.2.3	Results and discussion	33
4.3	Conclusions	38
5	Summary	40

- Temmer, M. 2021, Living Reviews in Solar Physics, 18, 4
- Thernisien, A. 2011, The Astrophysical Journal Supplement Series, 194, 33
- Thernisien, A., Vourlidas, A., & Howard, R. 2009, Solar Physics, 256, 111
- Thompson, B. & Young, C. 2016, The Astrophysical Journal, 825, 27
- Thompson, B. c., Gurman, J., Neupert, W., et al. 1999, The Astrophysical Journal, 517, L151
- Thompson, B. J. & Myers, D. C. 2009, *Astrophys. J. Suppl.*, 183, 225
- Thompson, B. J., Plumkett, S. P., Gurman, J. B., et al. 1998, *grl*, 25, 2465
- Torsti, J., Valtonen, E., Lumme, M., et al. 1995, *Sol. Phys.*, 162, 505
- Trottet, G., Samwel, S., Klein, K.-L., Dudok de Wit, T., & Miteva, R. 2015, Solar Physics, 290, 819
- Tsurutani, B. T. 1985
- Tsurutani, B. T., Gonzalez, W. D., & Kamide, Y. 1997, *Surveys in geophysics*, 18, 363
- Vainio, R. & Laitinen, T. 2008, *Journal of Atmospheric and Solar-Terrestrial Physics*, 70, 467
- van Haarlem, M. P., Wise, M. W., Gunst, A., et al. 2013, *Astronomy & astrophysics*, 556, A2
- Verbeeck, C., Delouille, V., Mampaey, B., & De Visscher, R. 2014, *Astronomy and Astrophysics*, 561, A29
- Verbeke, C., Mays, M. L., Kay, C., et al. 2022, *Advances in Space Research*
- Veronig, A., Muhr, N., Kienreich, I., Temmer, M., & Vršnak, B. 2010, *The Astrophysical Journal Letters*, 716, L57
- Vourlidas, A., Lynch, B. J., Howard, R. A., & Li, Y. 2013, *Solar Physics*, 284, 179
- Vourlidas, A., Syntelis, P., & Tsinganos, K. 2012, *Solar Physics*, 280, 509
- Vourlidas, A., Wu, S. T., Wang, A. H., Subramanian, P., & Howard, R. A. 2003, *apj*, 598, 1392
- Vršnak, B. & Cliver, E. W. 2008, *Solar Physics*, 253, 215
- Vršnak, B., Žic, T., Vrbanec, D., et al. 2013, *Solar physics*, 285, 295
- Warmuth, A. 2015, *Living Reviews in Solar Physics*, 12, 1
- Webb, D. F. & Howard, T. A. 2012, *Living Reviews in Solar Physics*, 9, 1
- Whitman, K., Egeland, R., Richardson, I. G., et al. 2023, *Advances in Space Research*, 72, 5161, cOSPAR Space Weather Roadmap 2022: Scientific Research and Applications
- Wild, J. & McCready, L. 1950, *Australian Journal of Chemistry*, 3, 387
- Wild, J., Smerd, S., & Weiss, A. 1963, *Annual Review of Astronomy and Astrophysics*, 1, 291
- Wills-Davey, M., DeForest, C., & Stenflo, J. O. 2007, *The Astrophysical Journal*, 664, 556
- Wöllmer, M., Zhang, Z., Weninger, F., Schuller, B., & Rigoll, G. 2013, in 2013 IEEE International Conference on Acoustics, Speech and Signal Processing, IEEE, 6822–6826
- Wood, B., Howard, R., & Socker, D. 2010, *The Astrophysical Journal*, 715, 1524
- Wu, C.-C. & Lepping, R. P. 2016, *Solar Physics*, 291, 265
- Wuelser, J.-P., Lemen, J. R., Tarbell, T. D., et al. 2004, in Society of Photo-Optical Instrumentation Engineers (SPIE) Conference Series, Vol. 5171, Telescopes and Instrumentation for Solar Astrophysics, ed. S. Fineschi & M. A. Gummin, 111–122

List of Tables

List of Figures

- 1.1 On the left side, a graphical illustration, adapted from ESA/A. Baker, CC BY-SA 3.0 IGO, depicts different eruptive phenomena, while on the right side, there is a representation of spacecraft data (specifically Wind/Waves data from Gopalswamy et al. (2019)) showcasing a radio dynamic spectra, emphasizing distinct spectral categories of SRBs on November 9, 2000. Type-II bursts are correlated with the shock front of a CME, whereas Type-IIIIs are connected with the acceleration of SEPs. Image courtesy¹
- 2
- 1.2 Composite image from the AIA and LASCO telescopes on the NASA-GSFC SDO and NASA/ESA SOHO spacecrafts shows a large CME being ejected to the east and its typical structure.
- 4
- 1.3 Classification of solar radio bursts
- 5
- 1.4 Coronagraph image captured by the SOHO/LASCO C3 instrument during a Halo-CME event. The speckled appearance of the corona results from signal contamination due to particles generated when SEPs interact with the SOHO telescope.
- 6
- 2.1 Illustration for the annulus method used to extract kinematic data from AIA images. (A) shows the full Sun disk with the relevant region highlighted for analysis (green sector). The white box outlines the AIA FOV. (B) displays the extracted annular region mapped onto polar coordinates, with the actual data extent marked by the white curve. Black lines indicate the directions used for measuring radial and lateral motions. (C) shows a stacked plot of intensity along the radial direction, with green markers highlighting intensity peaks and their corresponding distances from the CBF waveform. The white lines represent the time interval during which the CBF is tracked within the AIA FOV. This figure is curated from (Kozarev et al. 2017).
- 9
- 2.2 Synthetic shock model divided into three segments; the cap zone in blue and the flank zones are in red and green.
- 11
- 2.3 AIA running-difference images capture a coronal wave evolving over 9 minutes near the Sun's western limb, exhibiting markedly changing intensity and structure as observed in 171, 193, and 211 Å.
- 12
- 2.4 Time-series kinematics of the CBF parameters for the front, peak, and back positions in the AIA FOV, with measurement uncertainties shown as small bars over the data points. The horizontal lines in the speed and acceleration panels denote the mean speeds and accelerations for the wave front, peak, and back with respective colors. The left and right columns represent the lateral kinematic measurements in the left and right flanks of the wave, respectively. The middle column represent the kinematic measurements in the radial direction.
- 13
- 2.5 Top panel – Height-time profile compiled from AIA and LASCO measurements for the event occurred on May 11, 2011, fitted with two CME kinematics models from the photosphere up to $17 R_{\odot}$. Middle panel – Difference between the fitting and the real observations. Bottom panel – Relative residuals in %.
- 14
- 2.6 Extrapolated radial kinematics for the event occurred on May 11, 2011, based on the ballistic model of Gallagher et al. (2003) up to $17 R_{\odot}$
- 15
- 2.7 Dynamic spectra of the EUV waves kinematics in the AIA FOV. The panels from the top to the bottom are the wave speeds, acceleration, mean intensity, and thickness. The left column is for the lateral left flank, the central column is for the radial direction, and the right column is for the lateral right flank.
- 16
- 2.8 Histograms of along-field-lines model plasma parameters in the solar corona for all the 26 events. The vertical dashed red lines are the mean values.
- 17

- Nitta, N. V., Schrijver, C. J., Liu, W., et al. 2013, *The Astrophysical Journal*, 776, 58
- Nyrmik, R. 2007, *Advances in Space Research*, 40, 321
- Núñez, M. 2011, *Space Weather*, 9
- Odstrcil, D., Riley, P., & Zhao, X. 2004, *Journal of Geophysical Research: Space Physics*, 109
- Offringa, A. R., McKinley, B., Hurley-Walker, N., et al. 2014, *Mon. Not. R. Astron. Soc.*, 444, 606
- Ofman, L. & Thompson, B. 2002, *The Astrophysical Journal*, 574, 440
- Olah, C. 2015, *Neural Networks, Types, and Functional Programming*, [Blog post]
- Olmedo, O., Vourlidas, A., Zhang, J., & Cheng, X. 2012, *The Astrophysical Journal*, 756, 143
- Ontiveros, V. & Vourlidas, A. 2009, *The Astrophysical Journal*, 693, 267
- Ontiveros, V. & Vourlidas, A. 2009, *apj*, 693, 267
- Pala, Z. & Atici, R. 2019, *Solar Physics*, 294, 50
- Paouris, E., Vourlidas, A., Papaioannou, A., & Anastasiadis, A. 2021, *Space Weather*, 19, e2020SW002617
- Papaioannou, A., Anastasiadis, A., Kouloumvakos, A., et al. 2018, *Solar Physics*, 293, 1
- Papaioannou, A., Vainio, R., Raukunen, O., et al. 2022, *Journal of Space Weather and Space Climate*, 12, 24
- Park, J., Innes, D. E., Bucik, R., & Moon, Y.-J. 2013, *The Astrophysical Journal*, 779, 184
- Parker, E. N. 1960, *Astrophysical Journal*, 132, 821
- Patsourakos, S. & Vourlidas, A. 2009, *The Astrophysical Journal*, 700, L182
- Patsourakos, S. & Vourlidas, A. 2012, *Solar Physics*, 281, 187
- Patsourakos, S., Vourlidas, A., & Stenborg, G. 2010, *Astrophys. J. Lett.*, 724, L188
- Pérez-Suárez, D., Higgins, P. A., Bloomfield, D. S., et al. 2011, *Automated Solar Feature Detection for Space Weather Applications*, 207–225
- Pesnell, W. D., Thompson, B. J., & Chamberlin, P. C. 2012, *solphys*, 275, 3
- Piantschitsch, I., Vršnak, B., Hanslmeier, A., et al. 2018, *The Astrophysical Journal*, 860, 24
- Pick, M. 2006, in *Solar and Heliospheric Origins of Space Weather Phenomena*, ed. J.-P. Rozelot, Vol. 699, 119
- Pick, M., Forbes, T. G., Mann, G., et al. 2006, *Multi-Wavelength Observations of CMEs and Associated Phenomena*, Vol. 21, 341
- Podladchikova, O. & Berghmans, D. 2005, *Solar Physics*, 228, 265
- Pomoell, J. & Poedts, S. 2018, *Journal of Space Weather and Space Climate*, 8, A35
- Priest, E. & Forbes, T. 2007, *Magnetic Reconnection*
- Pulkkinen, T. 2007, *Living Reviews in Solar Physics*, 4, 1
- Pulupa, M., Bale, S., Bonnell, J., et al. 2017, *Journal of Geophysical Research: Space Physics*, 122, 2836
- Pulupa, M., Bale, S. D., Badman, S. T., et al. 2020, *Astrophys. J. Suppl.*, 246, 49
- Qiu, S., Zhang, Z., Yousof, H., et al. 2022, *Advances in Space Research*, 70, 2047
- Ramstad, R., Holmström, M., Futaana, Y., et al. 2018, *Geophysical Research Letters*, 45, 7306
- Reames, D. V. 1999, *Space Science Reviews*, 90, 413

4.2	Architecture of a single BiLSTM layer. The blue circles at the bottom labeled by $(x_0, x_1, x_2, \dots, x_i)$ are the input data values at multiple time steps. The purple circles, on the other hand, are the output data values at multiple time steps labeled by $(y_0, y_1, y_2, \dots, y_i)$. The dark green and light green boxes are the activation units of the forward and backward layers, respectively. The orange and yellow circles are the hidden states at the forward and backward layers, respectively. Both the forward and backward layers composes a single hidden BiLSTM layer. The figure is adopted from Olah (2015)	33
4.3	Benchmarking of 10 models, shows the Huber loss for the validation and test sets.	33
4.4	<i>Left Panel</i> - The Huber loss vs. the number of training epochs for the BiLSTM model for the validation and test sets, for the 3 energy channels. <i>Middle Panel</i> - The mean absolute error (MAE); the model's metric vs. the number of training epochs. <i>Right Panel</i> - Shows how the learning rate of the Adam optimizer changes over the number of epochs.	34
4.5	Correlation between the model predictions and observations for 1-day, 2-day, and 3-day ahead for >10 MeV (top panel), >30 MeV (middle panel), and >60 MeV (bottom panel). The panels in the left column represent all the points of the test set, those in the right column represent all the observations points with daily mean flux ≥ 10 pfu.	35
4.6	Comparison between the model outputs and observations of the test set for the 3 energy channels. In addition to the rolling-mean window correlation for 1-day ahead predictions.	36
4.7	The model's forecasts for the out-of-sample testing set for the >10 MeV channel are shown at forecast horizons of 1 day, 2 days, and 3 days ahead, using samples of data from December in selected years mentioned in the top-left side of the plots.	37
4.8	Temporal heatmap shows a comparison between the model outputs and observations for the rolling-mean window correlation of the integral >10 MeV proton flux at six predicting windows. The top panel represents the validation set and the bottom panel represents the testing set. The numbers on the y-axis are the mean R values.	38
4.9	Comparison between the model's forecast and the observations for the integral >10 MeV proton flux at forecast horizon of 1 hour ahead. The top panel represents a sample of the validation set and the bottom panel represents a sample of the testing set.	39
	Klassen, A., Karlický, M., & Mann, G. 2003a, <i>Astronomy & Astrophysics</i> , 410, 307	
	Klassen, A., Pohjolainen, S., & Klein, K.-L. 2003b, <i>Solar Physics</i> , 218, 197	
	Klein, K.-L. & Dalla, S. 2017, <i>Space Science Reviews</i> , 212, 1107	
	Kolen, J. F. & Kremer, S. C. 2001, Gradient Flow in Recurrent Nets: The Difficulty of Learning LongTerm Dependencies (IEEE), 237–243	
	Kong, X., Guo, F., Giacalone, J., Li, H., & Chen, Y. 2017, <i>The Astrophysical Journal</i> , 851, 38	
	Kontar, E. P., Chen, X., Chrysaphi, N., et al. 2019, <i>The Astrophysical Journal</i> , 884, 122	
	Kontar, E. P., Emslie, A. G., Clarkson, D. L., et al. 2023, arXiv preprint arXiv:2308.05839	
	Kontar, E. P., Yu, S., Kuznetsov, A., et al. 2017, <i>Nature communications</i> , 8, 1515	
	Kouloumvakos, A., Rodríguez-García, L., Gieseler, J., et al. 2022, <i>Frontiers in Astronomy and Space Sciences</i> , 9, 974137	
	Kozarev, K., Nedal, M., Miteva, R., Dechev, M., & Zucca, P. 2022, <i>Frontiers in Astronomy and Space Sciences</i> , 9, 34	
	Kozarev, K. A., Davey, A., Kendrick, A., Hammer, M., & Keith, C. 2017, <i>Journal of Space Weather and Space Climate</i> , 7, A32	
	Kozarev, K. A., Dayeh, M. A., & Farahat, A. 2019, <i>The Astrophysical Journal</i> , 871, 65	
	Kozarev, K. A., Evans, R. M., Schwadron, N. A., et al. 2013, <i>The Astrophysical Journal</i> , 778, 43	
	Kozarev, K. A., Korreck, K. E., Lobzin, V. V., Weber, M. A., & Schwadron, N. A. 2011, <i>The Astrophysical Journal</i> , 733, L25	
	Kozarev, K. A., Raymond, J. C., Lobzin, V. V., & Hammer, M. 2015, <i>The Astrophysical Journal</i> , 799, 167	
	Kozarev, K. A. & Schwadron, N. A. 2016, <i>apj</i> , 831, 120	
	Krucker, S., Hudson, H. S., Jeffrey, N. L. S., et al. 2011, <i>The Astrophysical Journal</i> , 739, 96	
	Krupar, V., Szabo, A., Maksimovic, M., et al. 2020, <i>Astrophys. J. Suppl.</i> , 246, 57	
	Kwon, R.-Y., Zhang, J., & Olmedo, O. 2014, <i>The Astrophysical Journal</i> , 794, 148	
	Laitinen, T. & Dalla, S. 2017, <i>The Astrophysical Journal</i> , 834, 127	
	Lakhina, G. S. & Tsurutani, B. T. 2016, <i>Geoscience Letters</i> , 3, 1	
	Lanzerotti, L. J. 2001, Washington DC American Geophysical Union Geophysical Monograph Series, 125, 11	
	Lavasa, E., Giannopoulos, G., Papaioannou, A., et al. 2021, <i>Solar Physics</i> , 296, 107	
	Le, G.-M. & Zhang, X.-F. 2017, <i>Research in Astronomy and Astrophysics</i> , 17, 123	
	Lecacheux, A., Steinberg, J. L., Hoang, S., & Dulk, G. A. 1989, <i>Astron. Astrophys.</i> , 217, 237	
	Lemen, J. R., Akin, D. J., Boerner, P. F., et al. 2011, in <i>The solar dynamics observatory</i> (Springer), 17–40	
	Lemen, J. R., Title, A. M., Akin, D. J., et al. 2012, <i>Solar Physics</i> , 275, 17	
	Li, B. & Cairns, I. H. 2012, <i>The Astrophysical Journal</i> , 753, 124	
	Lilensten, J., Coates, A. J., Dehant, V., et al. 2014, <i>The Astronomy and Astrophysics Review</i> , 22, 1	
	Lin, R. 2005, <i>Advances in Space Research</i> , 35, 1857	
	Liu, W. & Ofman, L. 2014, <i>Solar Physics</i> , 289, 3233	

Definitions and Acronyms

Here, I provide definitions for key domain-specific terms and measurement concepts throughout the thesis. Additionally, relevant terminology will be introduced within the corresponding chapters. Below is a compilation of the essential terms and acronyms defined in this work:

Gopalswamy, N. & Yashiro, S. 2011, apj, 736, L17
Gopalswamy, N., et al. 2022b, Journal of Geophysical Research: Space Physics,
127, e2022JA030404
Graves, A. & Jathay, N. 2014a (Beijing, China: PM&R), 1764-1772

Gopalswamy, N., Akhyama, S., Yasuno, S., Michalek, G., & Leppiing, R. 2008, Journal of Atmospheric and Solar-Terrestrial Physics, 70, 345

Gopalaswamy N., Mikkeli P., Yashiro S., et al. 2017in · Top Publishing · 012009

Gopalaswamy, N., Mallela, P., Yashiro, S., et al. 2017in , IOP Publishing, 012009

[97-EP22]A030404
Geopalaswamy, N., Yasuhiro, S., Akiryama, S., et al. 2022b, Journal of Geophysical Research: Space Physics,

on neural networks and learning systems, 28, 2222

Harris, C., 12; Brooks, D. H.; Bale, S. D., et al., 2021, Astroponomy & Astrophysics, 3, 35

Huang, X., Tan, H., Lin, G., & Tian, Y. 2018, 2018 International Conference on Artificial Intelligence (CAIP), (ICAIP) 2018

Helleland, J., Higginis, A. R., Shih, A. Y., et al. 2019, Solar Physics, 294, 158

Jamag, S., Moon, Y.-J., Kim, R.-S., Lee, H., & Cho, K.-S. 2016, The Astrophysical Journal, 820, 120

Kammer, S.; Chivre, E.; Chai, H., et al. 1981, in Proceedings of the 20 International Cosmic Ray Conference Moscow, Volume 3, p. 121

Kasapis, S., Zhao, L., Chen, Y., et al. 2022, Space Weather, 20, e2021SW002842

Kimigama, D. P. & Ba, J. 2015, International Conference on Learning Representations (ICLR), San Diego

GOFES	Geostationary Operational Environmental Satellite
LOFAR	Low-Frequency Array
SC	Solar Cycle
AU	Astromagnetic Unit
PLI	Proton flux unit
L1	First Lagrange point
SPDF	Space Physics Data Facility
SSLSO	Smooth Index and Long-term Solar Observations
NOAA	National Oceanic and Atmospheric Administration
GSFC	Goddard Space Flight Center
ESA	European Space Agency
MHD	Magnetohydrodynamic
MAS	Magnetohydrodynamic Algorithm outside a Sphere
PSI	Predictive Science Inc.
PPSS	Potential Field Source Surface
SPREDAST	Solar Particle Radiation Environment Analysis and Forecasting—Acceleration and Synthesis Transfer
DEM	Differential Emissivity Measure
NN	Neural Network
ML	Machine Learning
DL	Deep Learning
CNN	Convolutional Neural Network
RNN	Recurrent Neural Network

BiLSTM – Bi-directional Long short-term Memory
 Adam – Adaptive moment estimation
 MIMO – Multi-Input Multiple Output
 MSE – Mean Squared Error
 MAE – Mean Absolute Error
 MSLE – Mean Squared Logarithmic Error
 TP – True Positive
 TN – True Negative
 FP – False Positive
 FN – False Negative
 POD – Probability of Detection
 POFD – Probability of False Detection
 FAR – False Alarm Rate
 CSI – Critical Success Index
 TSS – True Skill Statistic
 HSS – Heidke Skill Score

- Che, H. 2018, Journal of Physics: Conference Series, 1100, 012005
 Chen, N., Ip, W.-H., & Innes, D. 2013, *Astrophys. J.*, 769, 96
 Chen, P. 2016, Low-Frequency Waves in Space Plasmas, 379
 Chen, P. F., Wu, S. T., Shibata, K., & Fang, C. 2002, *The Astrophysical Journal*, 572, L99
 Chen, X., Kontar, E. P., Chrysaphi, N., et al. 2023, arXiv e-prints, arXiv:2306.09160
 Cheung, M. C., Boerner, P., Schrijver, C., et al. 2015, *The Astrophysical Journal*, 807, 143
 Chhabra, S., Klimchuk, J. A., & Gary, D. E. 2021, *The Astrophysical Journal*, 922, 128
 Dalla, S., Swalwell, B., Battarbee, M., et al. 2017in (Cambridge University Press), 268–271
 Debrunner, H., Flückiger, E., Grädel, H., Lockwood, J., & McGuire, R. 1988, *Journal of Geophysical Research: Space Physics*, 93, 7206
 Delannée, C. & Aulanier, G. 1999, *Solar Physics*, 190, 107
 Dierckxsens, M., Tziotziou, K., Dalla, S., et al. 2015, *Solar Physics*, 290, 841
 Domingo, V., Fleck, B., & Poland, A. I. 1995, *Solar Physics*, 162, 1
 Dulk, G., Steinberg, J.-L., Lecacheux, A., Hoang, S., & MacDowall, R. J. 1985, *Astronomy and Astrophysics*, 150, L28
 Dungey, J. 1961, *Journal of Geophysical Research*, 66, 1043
 Eastwood, J., Nakamura, R., Turc, L., Mejnertsen, L., & Hesse, M. 2017, *Space Science Reviews*, 212, 1221
 Echer, E. & Gonzalez, W. 2022, *Advances in Space Research*, 70, 2830
 Echer, E., Tsurutani, B., & Gonzalez, W. 2013, *Journal of Geophysical Research: Space Physics*, 118, 385
 Efron, B. 1979, *The Annals of Statistics*, 7, 1
 Engell, A., Falconer, D., Schuh, M., Loomis, J., & Bissett, D. 2017, *Space Weather*, 15, 1321
 Ergun, R., Larson, D., Lin, R., et al. 1998, *The Astrophysical Journal*, 503, 435
 Feynman, J., Armstrong, T., Dao-Gibner, L., & Silverman, S. 1990, *Solar Physics*, 126, 385
 Fletcher, L., Dennis, B. R., Hudson, H. S., et al. 2011, *Space science reviews*, 159, 19
 Florios, K., Kontogiannis, I., Park, S.-H., et al. 2018, *Solar Physics*, 293, 28
 Fox, N., Velli, M., Bale, S., et al. 2016, *Space Science Reviews*, 204, 7
 Gabriel, S., Evans, R., & Feynman, J. 1990, *Solar physics*, 128, 415
 Gallagher, P. T., Lawrence, G. R., & Dennis, B. R. 2003, *The Astrophysical Journal Letters*, 588, L53
 Gieseler, J., Dresing, N., Palmroos, C., et al. 2023, *Frontiers in Astronomy and Space Sciences*, 9, 384
 Gonzalez, W., Joselyn, J.-A., Kamide, Y., et al. 1994, *Journal of Geophysical Research: Space Physics*, 99, 5771
 González, W. D., Echer, E., Clua-Gonzalez, A., & Tsurutani, B. T. 2007, *Geophysical research letters*, 34
 Goodfellow, I., Bengio, Y., & Courville, A. 2016, *Deep learning* (MIT press)
 Gopalswamy, N. 2022, *Atmosphere*, 13, 1781

Chapter 1

1.1 Background and Motivation

The aim of this thesis is to study the impact of solar flares and coronal mass ejections (CMEs) on the Earth's magnetosphere. This includes eruptive events like solar flares and CMEs, as well as various forms of activity on the Sun, such as耀斑 (Solar Flares) and coronal mass ejections (CMEs). The thesis is divided into two main parts: one focusing on the physical processes that lead to these events, and another focusing on their impact on the Earth's magnetosphere.

The first part of the thesis focuses on the physical processes that lead to solar flares and CMEs. It includes a detailed study of the different scales at which these events occur, from individual耀斑 to large-scale CMEs. The thesis also explores the physical mechanisms that drive these events, such as magnetic reconnection and plasma instabilities. The results of this part of the thesis provide a better understanding of the physical processes that lead to solar flares and CMEs, and how they can be predicted and mitigated.

The second part of the thesis focuses on the impact of solar flares and CMEs on the Earth's magnetosphere. It includes a detailed study of the different physical processes that are triggered by these events, such as particle acceleration and energy dissipation. The thesis also explores the impact of these events on various space weather phenomena, such as geomagnetic storms and auroras. The results of this part of the thesis provide a better understanding of the impact of solar flares and CMEs on the Earth's magnetosphere, and how they can be monitored and mitigated.

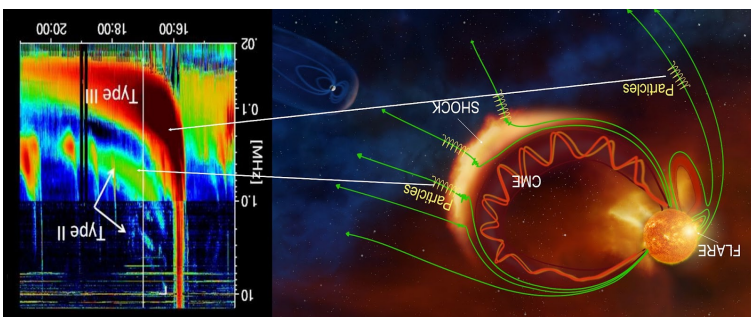


Figure 11: On the left side, a grayscale illustration of a CME, whereas Type-IIIs are connected with the acceleration of SEPs. Image courtesy of S. J. M. Zurbuchen.

- The Sun, a typical star at the centre of our solar system, displays various forms of activity across different scales. This includes magnetic triplite vortices like solar flares and Coronal Mass Ejections (CMEs), driven by the release of magnetic energy stored in complex magnetic structures in the solar corona. At the same time, the Sun undergoes periodic eruptions of various forms of activity across different scales. This includes magnetic triplite vortices like solar flares and Coronal Mass Ejections (CMEs), driven by the release of magnetic energy stored in complex magnetic structures in the solar corona. These eruptions, often referred to as solar flares or CMEs, can have significant impacts on Earth and space weather. For example, they can cause geomagnetic storms, which can disrupt satellite communications, power grids, aviation, and space missions (Lazarro et al., 2001; Schwenn, 2006; Pulkkinen, 2007; Lilensten et al., 2014).

Understanding these solar phenomena and their impacts is crucial for global safety. Research aims to uncover the underlying physical processes through observational studies. This field, known as heliophysics (Schrijver & Zee, 2010b), encompasses studies of the Sun, heliosphere, and geospace plasma processes, their impacts on technology and space weather, and strategies for prevention and mitigation (Schrijver et al., 2015). This focus on investigating key aspects of solar activity and its impacts within the framework of heliophysics and space weather. Specific topics include studying the propagation of coronal disturbances triggered by CMEs and flares, the characteristics of solar type III radio bursts, and forecasting space weather hazards.

Solar Energetic Particle (SEP) events, which pose significant space radiation hazards, are another class of heliophysics and space weather. SEP events are characterized by CMEs and flares, and their impacts within the framework of heliophysics and space weather. Specific topics include studying the propagation of coronal disturbances triggered by CMEs and flares, the characteristics of solar type III radio bursts, and forecasting space weather hazards.

Besides the Sun, other stars in the Milky Way also exhibit similar magnetic activity and coronal mass ejections. For example, the star Procyon exhibits periodic eruptions of various forms of activity across different scales, including solar flares and CMEs (Lazarro et al., 2001; Schwenn, 2006; Pulkkinen, 2007; Lilensten et al., 2014). The Sun's magnetic field is also influenced by the rotation of the star, which drives the solar cycle (Schrijver & Zee, 2010b).

The Sun's magnetic field is also influenced by the rotation of the star, which drives the solar cycle (Schrijver & Zee, 2010b). The Sun's magnetic field is also influenced by the rotation of the star, which drives the solar cycle (Schrijver & Zee, 2010b).

Figure 1.1: On the left side, a graphical illustration, adapted from ESA/A. Baker, CC BY-SA 3.0 IGO, depicts different eruptive phenomena, while on the right side, there is a representation of spacecraft data (specifically Wind/Waves data from October 9, 2019) showing a radio metric signature of a radio metric event with the shock front of a CME, whereas Type-III are connected with the acceleration of SEPs. Image courtesy of Glesener, L., Leitner, B., et al. 2021, *Astrophys. Space Phys.*, 650, A6

1.1 Background and Motivation

Computer Engineering (ICCCF), IEEE, 1–6

Allabhi, F. R., & Casla, D. 2021, in 2021 International Conference on Electrical, Communication, and SSSH

Amari, T., Chau, A., & Ali, J.-J. 2014, *Nature*, 514, 465

Aschwanden, M. J. 2002, *Space Science Reviews*, 101, 1

Aschwanden, M. J. 2010, *Solar Physics*, 262, 235

Badaoui, S., T., Carley, E., Chiarzee, L., et al. 2022, *The Astrophysical Journal*, 938, 95

Bale, S., Geetze, K., Harvey, P., et al. 2016, *Space science reviews*, 204, 49

Bastian, T., Pilk, M., Berkebile-Storer, S., Veronig, A. M., et al. 2011, *The Astrophysical Journal*, 558, 165

Battarbee, M., Vainio, R., Latini, T., & Hietala, H. 2013, *Astrophysics*, 558, A110

Besliu-Schuster, D., Myers, D., Thompson, B., Hammer, D., & Vourlidas, A. 2002, *The Astrophysical Journal*, 569, 1009

Bonini, X., Hoang, S., & Makisimovici, M. 2008, *Astrophys. Space Phys.*, 489, 419

Borovsky, J. E., & Deanton, M. H. 2006, *Journal of Geophysical Research: Space Physics*, 111

Boudjada, M. Y., Abou El Fadil, A., Galoppean, P. H., Al-Haddad, E., & Lammer, H. 2020, *Advances in Radio Science*, 18, 383

Bremer, D. A., Barth, J. L., Label, K. A., Kaufman, W. J., & Giffin, G. 2002, *Acta Astronautica*, 51, 699

Brynnel, J., Long, D., Gallagher, P., et al. 2013, *Astrophysics*, 557, A96

Cameron, H. V., Erickson, W., & Prestage, N. 2002, *Journal of Geophysical Research: Space Physics*, 107, 1166

Cattell, C., Glesener, L., Leitner, B., et al. 2021, *Astrophys. Space Phys.*, 650, A6

The thesis investigates the origins and propagation mechanisms of transient phenomena resulting from solar eruptions. It employs observational data, analytical theory, modeling, and data science techniques. Despite decades of study using space mission observations, gaps persist in understanding their underlying physics and space weather impacts. The thesis aims to provide new insights within the framework of heliophysics research. Each research topic is explored in dedicated chapters, discussing background, significance, observational challenges, knowledge gaps, and relevant literature. More details can be found in the thesis.

1.1.1 Coronal Waves

Coronal waves, also known as Coronal Bright Fronts (CBFs) or EUV waves, are large-scale arc-shaped disturbances observed propagating across the solar corona following the eruption of CMEs and solar flares (Thompson et al. 1998; Nindos et al. 2008; Vršnak & Cliver 2008; Magdalenić et al. 2010a; Veronig et al. 2010; Warmuth 2015). These waves, visible in EUV, white-light coronal emission, and radio wavelengths, can span distances of up to several hundred Mm and travel at speeds ranging between $100\text{--}1000 \text{ km s}^{-1}$, faster than the local characteristic speed in the corona, eventually transforming into shock waves (Pick et al. 2006; Thompson & Myers 2009; Nitta et al. 2013; Liu & Ofman 2014). They consist of piled-up plasma with higher density, making them appear brighter in white-light images.

Discovered through observations obtained with the Extreme ultraviolet Imaging Telescope (EIT) instrument on the Solar and Heliospheric Observatory (SOHO) that was launched in 1995, coronal waves appear as bright propagating fronts in 19.5 nm wavelength imaging of Fe XII emission lines formed at approximately 1.5 MK plasma (Thompson et al. 1998). Subsequent studies using SOHO/EIT and the Transition Region and Coronal Explorer (TRACE) found correlations between coronal waves and CMEs, suggesting they are fast-mode magnetohydrodynamic (MHD) waves driven by CME lateral expansions (Biesecker et al. 2002).

Since 2010, the initiation and evolution of coronal waves have been observed with unprecedented resolution by the Atmospheric Imaging Assembly (AIA) on the Solar Dynamics Observatory (SDO), using multiple EUV passbands sensitive to a wide temperature range (Lemen et al. 2012; Nitta et al. 2013). Observing and studying coronal shock waves remotely is typically done through EUV observations using space-based instruments like AIA onboard the SDO spacecraft. Alternatively, shock waves can be indirectly observed through the detection of type II radio bursts, commonly associated with shock waves in the solar corona (Vršnak & Cliver 2008).

The AIA instrument, with its exceptional spatial and temporal resolution, has provided significant insights into the dynamics of the low solar corona over the past decade (Patsourakos et al. 2010; Ma et al. 2011; Kozarev et al. 2011). By observing the solar disk in bands 193 and 211 Å, it distinguishes compressive waves in the lower corona, offering valuable information about the kinematics and geometric structure of CBFs. Observations off the solar limb are preferred to study the evolution of the wave's leading front accurately, mitigating projection effects that may introduce ambiguities (Kozarev et al. 2015).

CMEs typically consist of three parts (Fig. 1.2): the CME Front, CME Cavity, and CME Core (Vourlidas et al. 2013). CBFs form in front of the expanding front of CMEs. In situ observations of shock waves classify them into quasi-parallel, quasi-perpendicular, sub-critical, and super-critical shocks based on the angle between the wavefront normal vector and the upstream magnetic field lines (Tsurutani 1985). Coronal waves display diverse morphology and kinematics, ranging from circular fronts to narrow jets or expanding dome-like structures (Veronig et al. 2010). However, fundamental questions persist regarding their physical nature and drivers (Chen 2016; Vršnak & Cliver 2008; Warmuth 2015), including whether they are true wave disturbances or pseudo-wave fronts (Wills-Davey et al. 2007; Vršnak & Cliver 2008; Delanée & Aulanier 1999; Chen et al. 2002).

Extensive observational and modeling studies have been conducted to evaluate these paradigms, but a consensus remains elusive (Patsourakos & Vourlidas 2012; Long et al. 2017). Addressing these outstanding questions is crucial, as coronal waves are being incorporated into models as primary agents producing SEP events and geomagnetic storms following CMEs (Rouillard et al. 2012; Park et al. 2013). The present thesis undertakes an extensive statistical analysis of coronal EUV wave events observed by SDO to provide new insights into their kinematical properties and relationship to CMEs and plasma properties in the corona. It focuses on analyzing their large-scale evolution as a function of distance and direction from the source region, aiming to uncover systematic trends in their propagation kinematics and exploring relationships between different pairs of kinematical parameters compared to previous works.

¹<https://www.dias.ie/cosmicphysics/astrophysics/astro-surround/>

Chapter 5

Summary

In this final chapter, I provide a comprehensive summary of key findings from the dissertation's chapters, focusing on EUV waves, solar type III bursts, and SEP modeling and forecasting. Exploration of CBFs and the Wavetrack tool enhances understanding of solar dynamics. Extending the CBF dataset promises deeper insights, while multi-wavelength observations aim to elucidate energetic particle origins. Developments in interpretable deep learning models driven by higher resolution data offer potential for advancing SEP forecasting.

Chapter 2 analyzes base-difference images from SDO/AIA to study EUV waves, calculating kinematic parameters and employing SOHO/LASCO measurements, and exploring the plasma parameters during the propagation of CBFs. Chapter 3 examines type III bursts during PSP's near-Sun encounters, observing sixteen bursts using PSP/FIELDS and LOFAR. A semi-automated pipeline aids in data analysis, aligning bursts and locating emissions off the southeast limb, suggesting a single source of electron beams low in the corona. Chapter 4 introduces a BiLSTM NN model for forecasting SEP integral flux at 1 AU shows promising results for short-term predictions.

In conclusion, the dissertation contributes to understanding EUV waves, provides insights into type III bursts and SEP simulations, and advances forecasting using deep learning. Future directions include refining models and incorporating recent data for comprehensive space weather forecasting.

The quest to understand the Sun's dynamic nature persists, with future heliophysics research poised to advance our knowledge and space weather forecasting capabilities.

Expanding the dataset for EUV waves across solar cycle phases offers insights into their behavior amidst cyclical solar activity. Similarly, analyzing solar radio bursts across diverse active regions enhances our understanding of their characteristics. Utilizing multi-wavelength observations from instruments like LOFAR, PSP, and Solar Orbiter enriches our understanding of energetic particles and radio bursts in the solar corona. High-resolution data enhances the accuracy of dynamic process representations. Addressing scattering and propagation effects on SEPs and radio burst observations is crucial for refining forecasting models.

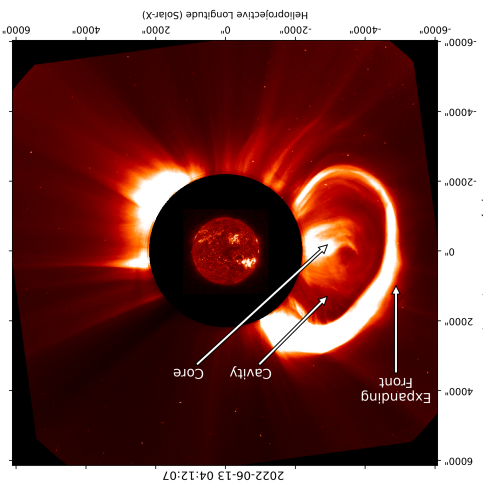
Incorporating features from active regions into SEP prediction models improves forecasting capabilities. Implementing interpretable deep learning architectures enhances model reliability and reduces forecasting errors. Developing real-time analysis tools integrating data from new instruments and space-craft, alongside advanced methodologies, enables early warnings and accurate risk assessments for space weather events.

Type III bursts manifest as intense enhancements of radio flux with rapid frequency drifts, whereas Type III bursts maintain form from GHz to kHz (Widl & McCready 1985; Lebreton et al. 1989; Bonham et al. 2008). They arise from energetic electrons affected during magnetic reconnection, with the rapid drift corresponding to the beams' propagation along the Sun's lower corona outward along plasma environments, and beam kinematics is vital for understanding coronal particle acceleration and transport models.

Pioneering observations in the 1940s led to the classification and subsequent spectrographic studies of solar radio bursts, uncovering emission mechanisms and particle diagnostic tools (Widl et al. 1963; Suzuki et al. 2003a,b). Different burst types are observed and classified based on their sources on the Sun, offering insights into the physical transport from the Sun to Earth (Frucker et al. 2011; Klassen et al. 1963), with this focus on a detailed analysis of spectral characteristics (Fig. 13). Different burst types are observed and classified based on their sources on the Sun, offering insights into the physical transport from the Sun to Earth (Frucker et al. 2011; Klassen et al. 1963), with this focus on a detailed analysis of spectral characteristics (Fig. 13). Different burst types are observed and classified based on their sources on the Sun, offering insights into the physical transport from the Sun to Earth (Frucker et al. 2011; Klassen et al. 1963), with this focus on a detailed analysis of spectral characteristics (Fig. 13).

1.2 Solar Radio Bursts

Figure 12: Composite image from the AIA and LASCO telescopes on the NASA-GSFC SDO and NASA/ESA SOHO spacecrafts shows a large CME being effected to the east and its typical structure. These results have important implications for incorporating coronal waves into predictive models of CMEs and SEP events for future space weather forecasting.



BLSTM networks offer a promise for heliophysics forecasting tasks, warranting future investigation into optimal model configurations and data requirements. Our study contributes to the growing field of deep learning in heliophysics and space weather research.

Figure 4.9: Comparison between the models' forecast and the observations for the magnetar > 10 MeV proton flux at forecast horizon of 1 month ahead. The top plot represents a sample of the validation set and the bottom panel represents a sample of the testing set.

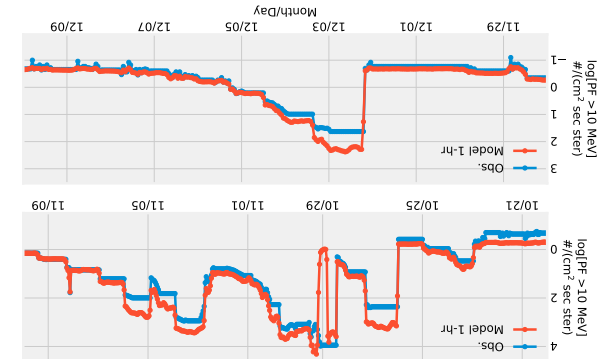


Figure 4.9: Comparison between the models' forecast and the observations for the magnet > 10 M GeV proton flux at forecast horizon of 1 day ahead. The top row represents a sample of the validation set and the bottom panel represents a sample of the testing set.

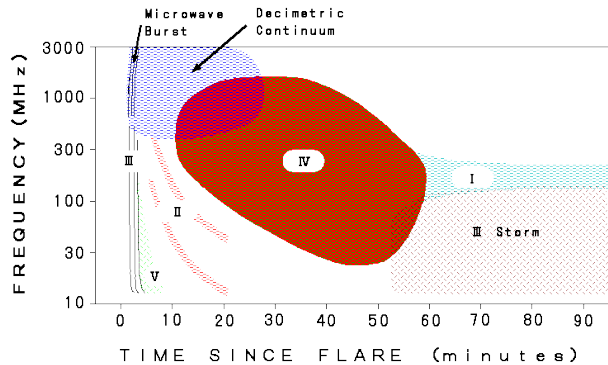


Figure 1.3: Diagram illustrating the classification of solar radio bursts. Image courtesy²

exciters in detail (Chen et al. 2013; Kontar et al. 2017), yet challenges remain in reconciling models with observations and predicting radio diagnostics. Coordinated observations and modeling efforts can advance knowledge in these areas, aiding predictions of energetic electron properties based on radio diagnostics. This thesis undertakes a detailed investigation of a solar type III burst, deriving electron beam trajectories, coronal densities, and emission sources, providing insights into the corona plasma environment and energetic electron transport relevant to SEP forecasting applications.

1.1.3 Solar Energetic Protons Forecasting

Solar energetic protons (SEPs) are high-energy particles originating from solar flares and CMEs, characterized by their high energy levels (up to the GeV/nucleon range) and potential to cause radiation damage (Aschwanden 2002; Lin 2005; Reames 2013). Their fluence and energy spectrum depend on various factors, including solar activity strength and interplanetary conditions (Kahler et al. 1984, 1987; Debrunner et al. 1988; Mitev et al. 2013; Trottet et al. 2015; Dierckxsems et al. 2015; Le & Zhang 2017; Gopalswamy et al. 2017). SEPs exhibit a strong association with the solar cycle, peaking during its maximum phase (Reames 2013), although the exact relationship remains complex and not fully understood (Nyrmik 2007; Ramstad et al. 2018).

Figure 1.4 illustrates the impact of SEPs during the *Halloween storm* of 2003, a significant solar event. SEPs play a crucial role in adverse space weather, posing radiation hazards to humans and equipment in space (Reames 1999). SEP events consist primarily of protons accelerated by CME-driven shock waves, with gradual events involving protons above ~ 10 MeV and impulsive events dominated by electrons and ions like ${}^3\text{He}$ (Reames 2013; Nitta et al. 2015).

SEP forecasting models face challenges due to the complex physics involved, motivating the exploration of data-driven approaches using machine learning (Kahler et al. 2007; Laitinen & Dalla 2017). Deep learning techniques offer promising avenues for improved predictions, capturing complex relationships between parameters (Florios et al. 2018; Camporeale 2019). This thesis aims to develop deep Neural Network models for predicting SEP intensity profiles, leveraging historical data to enhance forecasting capabilities.

1.2 Objectives and Scope

This PhD thesis explores various solar phenomena, including CBFs, type III radio bursts, and SEP events, aiming to deepen our understanding of solar corona physics and its relation to eruptions and energetic particle radiation.

For CBFs, the research analyzes 26 historical events observed by the AIA instrument on SDO from 2010 to 2017, examining their properties and kinematics in relation to the coronal plasma environment.

²Types of solar radio bursts: http://solar.physics.montana.edu/takeda/radio_burst/srb.html

Short-term Forecasting

This study aims to enhance the prediction accuracy of SEP integral flux, crucial for mitigating space weather hazards (Nedal et al. 2023a). Employing a BiLSTM NN model, it utilizes high-resolution hourly-averaged data from four standard integral GOES channels. Key input parameters include the F10.7 index, sunspot number, x-ray flux, solar wind speed, and IP magnetic field strength, sourced from OMNIWeb and GOES databases across two solar cycles. Additional features, like active region locations from NOAA daily reports, are incorporated for improved predictions.

Evaluation involves out-of-sample testing, assessing feature impacts, and benchmarking against existing methods. Data partitioning follows the 9-2-1 strategy over a 23-year period (1996–2018), with 73.99%, 16.44%, and 9.57% allocated to training, validation, and testing sets respectively. Data formatting adopts the MIMO strategy (Benson et al. 2020).

The model forecasts the logarithm of integral proton flux across energy channels, with a focus on >10 MeV. Figure 4.9 compares 1-hour predictions with observations for two sample SEP events.

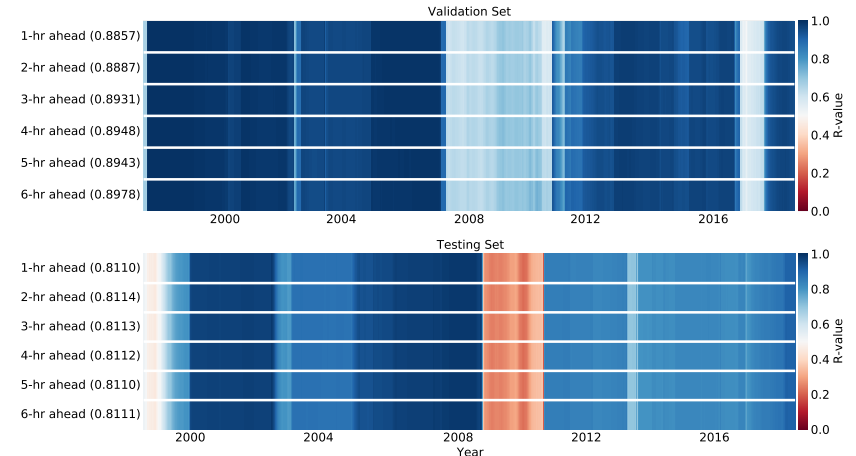


Figure 4.8: Temporal heatmap shows a comparison between the model outputs and observations for the rolling-mean window correlation of the integral >10 MeV proton flux at six predicting windows. The top panel represents the validation set and the bottom panel represents the testing set. The numbers on the y-axis are the mean R values.

Table 4.4: The MSE/MAE for the validation and test sets over six forecasting windows.

	1-hr	2-hr	3-hr	4-hr	5-hr	6-hr
Valid. Set	0.078/0.238	0.086/0.254	0.091/0.263	0.098/0.273	0.102/0.280	0.115/0.299
Test Set	0.012/0.080	0.012/0.079	0.012/0.080	0.011/0.079	0.011/0.080	0.011/0.079

4.3 Conclusions

In Nedal et al. (2023a), BiLSTM neural networks are developed and trained to predict daily-averaged integral flux of SEP at 1-day, 2-day, and 3-day ahead, focusing on energy channels >10 MeV, >30 MeV, and >60 MeV. Input data from OMNIWeb databases span four solar cycles, utilizing MIMO strategy for forecasting, achieving promising results with low MSE values and strong correlations.

The study highlights challenges in longer-term SEP forecasting, particularly in maintaining model performance over extended forecasting windows. Short-term predictions are crucial for space weather forecasting, emphasizing the significance of accurate modeling for protecting space assets.

This dissertation examines CFFs, solar radio bursts, and SEP events. It analyzes the kinematics of CFFs in the solar corona, investigating 26 CFFs associated with SEP events observed between 2010 and 2017. The study employs the SEPREADFAST framework to understand CFF kinematics and plasma parameters during space weather forecasts (Chapter 2). Additionally, it presents a method and structure orientation for accurate storm prediction. Chapter 3 focuses on the CME speed and magnetic field orientation of 16 bursts using multi-wavelength data from Type III radio bursts, analyzing the structure orientation for accurate storm prediction. Chapter 4 investigates the importance of considering CME speed and magnetic field orientation for accurate storm prediction. Chapter 5 summarizes the effectiveness of these models in validating through testing and developing forecasting models using a BILSTM framework. Finally, Chapter 6 summarizes the effectiveness of these models in validating through testing and developing forecasting models using a BILSTM framework.

1.3 Outlines

The study of type III radio bursts focuses on investigating their generation mechanisms, identifying the sources in the solar corona, and investigating specific features observed on April 3, 2019, using data from LOFAR and PSP instruments, comparing observations with existing models and exploring potential burst sources.

In EPF forecasting, the aim is to develop a BiLSTM neural network model capable of predicting daily EPF mega-flux within a three-day window for energy ranges > 10 MeV, < 10 MeV, and > 60 MeV. The model's performance is evaluated against established forecasting methods using historical SEP data from the past four solar cycles, assessing accuracy and effectiveness through various metrics. By addressing these aspects of solar activity, this research advances our understanding of solar flares and enhances our ability to predict space weather events impacting Earth.

Figure 14. Coronagraphic image captured by the SOHO/LASCO C3 instrument during a Hale-CME event. The speed of propagation of the coronal disturbance from the SOHO/SOHO-E region due to particles generated within SEPs interact with the SOHO-E region.

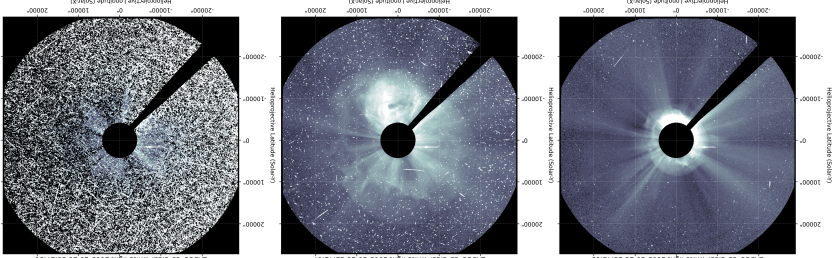
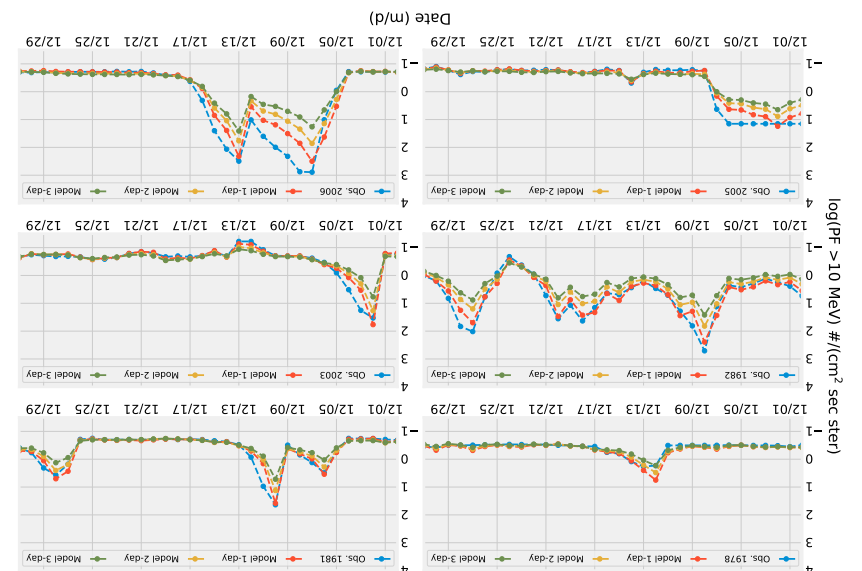


Figure 4f. The mode selection set for the out-of-sample testing set for the >10 MeV channel are shown at different time horizons of 1 day, 2 days, and 3 days, and using samples of data from December in selected years mentioned in the top-left side of the plots.



Chapter 2

Remote Observations

Early-stages and Later-stages of Eruption

This chapter covers three main topics related to EUV waves and CMEs. Firstly, it focuses on the kinematics of CBFs in both the lower and middle/outer coronas, along with an examination of coronal plasma conditions during these eruptions. Additionally, it discusses my contributions to testing and debugging the *Wavetrack* Python library, developed by Stepanyuk et al. (2022), for detecting and tracking solar features using wavelet transforms and filtering techniques. Lastly, it examines the research led by Miteva et al. (2023) regarding the connection between reconstructed 3D CME models and geomagnetic storm intensity, emphasizing the importance of accurate 3D modeling for space weather forecasting. The chapter will present the results of each topic individually, followed by a combined discussion and concluding remarks.

2.1 Introduction

CMEs are prominent indicators of solar activity, observable through various wavelengths including white light, UV, and radio (Vourlidas et al. 2003; Zhang & Dere 2006; Bein et al. 2011; Bastian et al. 2001; Veronig et al. 2010). Early CME phases are effectively observed in Extreme Ultraviolet (EUV) light, facilitated by instruments like AIA aboard SDO (Lemen et al. 2011; Pesnell et al. 2012). CMEs can induce shock waves in the solar corona, visible as EUV waves or CBFs (Thompson et al. 1998; Long et al. 2011).

CBFs are disturbances propagating over the solar disk and limb, often faster than local characteristic speeds, driven primarily by CMEs or solar flares (Thompson et al. 1998; Veronig et al. 2010; Vršnak & Cliver 2008; Magdalenić et al. 2010b; Nindos et al. 2011). They appear as dome-shaped structures in radio and white-light observations, composed of denser plasma and thus appearing brighter in images (Pick et al. 2006; Nindos et al. 2008; Thompson & Myers 2009).

Studies have clarified CBF characteristics both on the solar disk and off the limb, confirming their wave-like nature (Nitta et al. 2013; Long et al. 2011; Olmedo et al. 2012). Observations from instruments like LASCO onboard SOHO have extended shock wave investigations beyond $2.5 R_{\odot}$ (Domingo et al. 1995; Vourlidas et al. 2003). While EUV observations link CMEs and EUV waves, understanding shock waves in EUV remains incomplete (Patsourakos & Vourlidas 2009; Kozarev et al. 2011). Emission measure modeling using AIA's EUV channels provides insights into temperature and density changes in the wavefront's sheath (Kozarev et al. 2011). Multi-wavelength observations from SOHO/LASCO and SDO/AIA instruments have revealed valuable information about CBF properties near the Sun (Warmuth 2015). Factors such as nearby active regions or coronal holes can distort CBF morphology, and a connection between CBFs and chromospheric disturbances known as Moreton waves has been established (Ofman & Thompson 2002; Mann et al. 2003; Piantschitsch et al. 2018; Thompson et al. 1999). In this study, I analyzed 26 CBF events up to $\sim 17 R_{\odot}$ using observations and modeling tools from the Solar Particle Radiation Environment Analysis and Forecasting–Acceleration and Scattering Transport (SPREAdFAST) framework (Kozarev et al. 2022). The study aims to characterize CBF kinematics and estimate ambient plasma properties to understand the relationships between shock and plasma parameters.

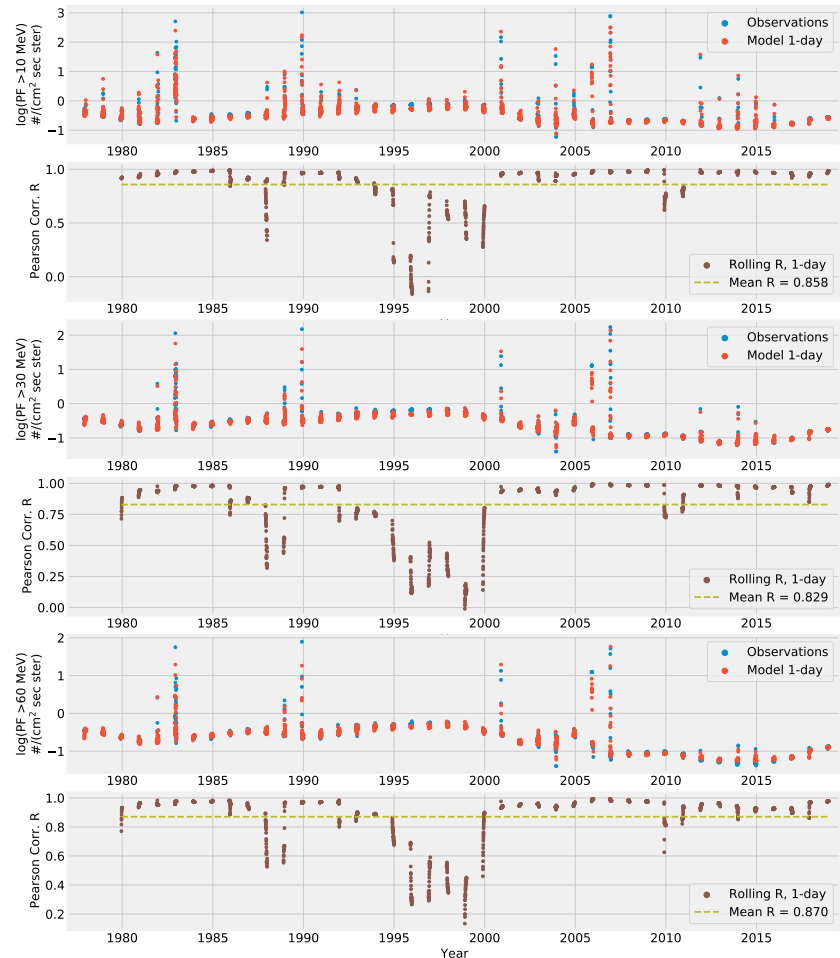


Figure 4.6: Comparison between the model outputs and observations of the test set for the 3 energy channels. In addition to the rolling-mean window correlation for 1-day ahead predictions.

To analyze the kinematics of CBFs, the Coronair Analysis of Shocks and Waves framework (Kazerooni et al. 2017; CASHEW) was employed. This semi-automated technique involved extracting similar regions from AIA images and mapping them onto polar projections (Fig. 2). By tracking intensity changes

The mean latitude and mean longitude of the CBFs were calculated as 56.35 and 378.04 arcsec, whereas the mean latitude and mean longitude of the CDFs were calculated as 56.35 and 378.04 arcsec. Additionally, the mean latitudes of CBFs in the northern and southern solar hemispheres were found to be 283.00 and -252.73 arcsec, respectively. As for the mean longitudes, they were 803.11 arcsec on the eastern and western sides, respectively, and 803.11 arcsec on the northern and southern sides, respectively. The mean latitudes of CDFs in the northern and southern solar hemispheres were found to be 283.00 and -252.73 arcsec, respectively. As for the mean longitudes, they were -775.71 and 803.11 arcsec on the eastern and western sides, respectively.

Detailed information about the selected events, including their start/end times, associated bars, and source locations on the solar disk, was obtained from the Heliophysics Events Knowledgebase (HEK). Notably, the mean latitude and longitude of the CMEs were calculated, along with their distribution across the solar hemisphere and quadrants. CMEs, observed as faint quasi-spherical sheets, were primarily visible in the 193 Å channel. To analyze their evolution, sequences of base-difference images were generated for each event, allowing us to track their propagation over time (Vourlidas et al. 2003; Opher et al. 2009; Piatzetti et al. 2011; Ma et al. 2011).

The selected variables (Table 2.1), previously discussed in (Kozorev et al. 2022), were further examined using imagemetry from the AIA instruments EUV channel 193 Å. These images, captured at a 24-second cadence, provided the primary input for our analysis within the SPREADFAST framework.

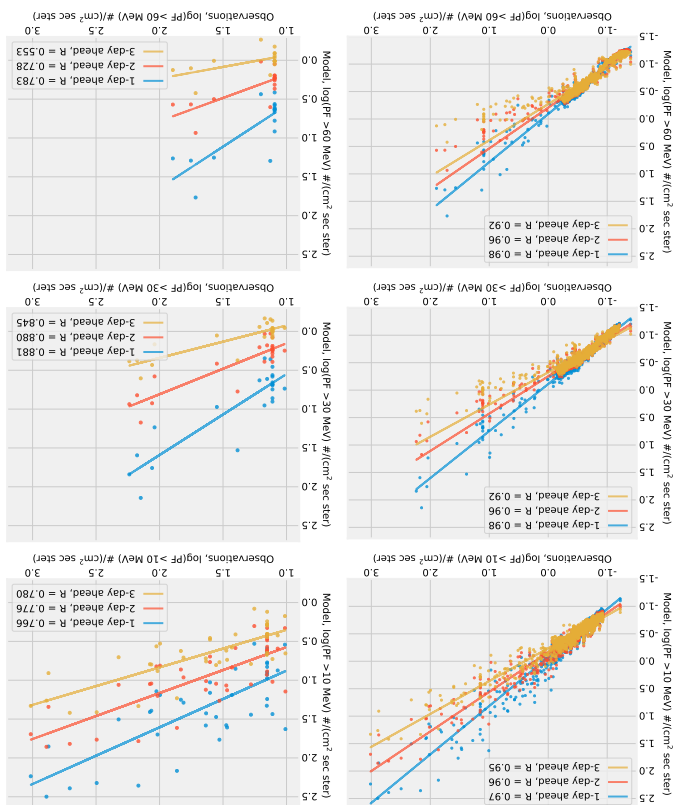
We conducted a study utilizing data from the SOHO/ERNE instrument, focusing on proton events with energies between 17–22 MeV, spanning from 2010 to 2017. Initially, 126 events were selected, but after the strictest selection criteria were applied, 133 events were excluded due to various factors such as the absence of EUV wave associated CMEs, or flares. This left us with a final set of 26 events for analysis.

2.2 EUV Observations

Table 2.1: List of the CBF events with their associated tides and CMES.

Model	POD	FAR	TSS	SSS	PoFD	CSI	Accuracy	Precision
Our BiLSTM model	0.618	0.121	0.531	0.732	0.001	0.583	0.99	0.913
1-Day	0.417	0.125	0.287	0.533	0.001	0.389	0.95	0.875
2-Day	0.412	0.125	0.287	0.533	0.001	0.389	0.95	0.875
3-Day	0.417	0	0.147	0.252	0	0.147	0.980	1
UMASPEF10 (Nineteen 2011)	0.822	0.129	—	—	—	—	—	—
PCA (Papadimitriou et al. 2018)	0.585	0.245	—	0.65	—	—	—	—
SPPNTS (Dabla et al. 2017)	0.5	0.37	—	—	0.32	0.3	—	—
SPRNTS (Engel et al. 2017)	0.36	0.34	—	—	0.58	—	—	—
RELASe (Malardrieux & Crosby 2018)	0.63	0.3	—	—	—	—	—	—

Table 4.3: Comparing the skill scores with previous models. The dashed entries mean the data unavailable (Whitman et al. [2023] for more details).



During low solar activity, forecasting low SEP fluxes becomes challenging due to increased randomness. Factors influencing correlation during quiet periods require further investigation.

Model performance ranked highest for >60 MeV, followed by >10 MeV and >30 MeV channels. Correlation decline at >30 MeV is consistent with previous findings (Le & Zhang 2017).

Visual inspection of test set examples (Fig. 4.5) revealed strong correlation between predicted and observed onset time, peak time, and end times of SEP events. This suggests that the model effectively captures temporal variations and flux trends in SEP events.

Evaluation using skill scores and threshold-based clustering algorithm demonstrated declining performance with longer forecasting windows. Our model showed comparable performance with previous studies (Table 4.3), with lower false alarm rate compared to UMASEP model.

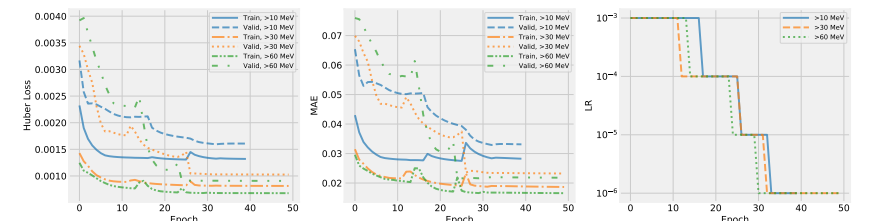


Figure 4.4: *Left Panel* - The Huber loss vs. the number of training epochs for the BiLSTM model for the validation and test sets, for the 3 energy channels. *Middle Panel* - The mean absolute error (MAE); the model's metric vs. the number of training epochs. *Right Panel* - Shows how the learning rate of the Adam optimizer changes over the number of epochs.

Table 4.1: Summary of the performance results of the models for the validation and test sets.

Validation Set								
	log PF >10 MeV			log PF >30 MeV			log PF >60 MeV	
Model Loss	0.0016			0.0010			0.0009	
Model Metric	0.0329			0.0232			0.0218	
	1-Day	2-Day	3-Day	1-Day	2-Day	3-Day	1-Day	2-Day
MAE	0.061	0.091	0.125	0.053	0.079	0.098	0.052	0.069
MSE	0.013	0.028	0.054	0.010	0.031	0.055	0.009	0.027
RMSE	0.114	0.168	0.233	0.098	0.176	0.234	0.097	0.164
MAPE	22.156	28.104	34.721	13.039	18.590	22.735	10.036	13.994
Test Set								
	log PF >10 MeV			log PF >30 MeV			log PF >60 MeV	
Model Loss	0.0014			0.0011			0.0010	
Model Metric	0.0333			0.0283			0.0250	
	1-Day	2-Day	3-Day	1-Day	2-Day	3-Day	1-Day	2-Day
MAE	0.072	0.099	0.125	0.053	0.088	0.107	0.045	0.066
MSE	0.015	0.030	0.050	0.009	0.029	0.048	0.007	0.020
RMSE	0.121	0.172	0.224	0.094	0.170	0.218	0.082	0.141
MAPE	30.135	37.498	48.139	20.599	34.300	40.803	12.358	20.504

Table 4.2: Confusion matrix for the energy channel ≥ 10 MeV predictions in the test set.

E >10 MeV	No. events	TP	TN	FP	FN
1-day ahead	15	21	1441	2	13
2-day ahead	13	14	1441	2	20
3-day ahead	5	5	1443	0	29

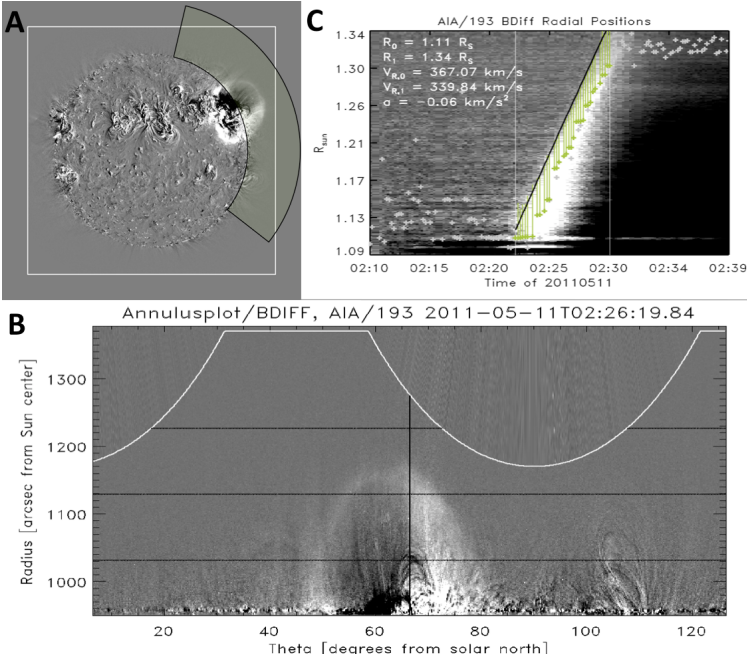


Figure 2.1: Illustration for the annulus method used to extract kinematic data from AIA images. (A) shows the full Sun disk with the relevant region highlighted for analysis (green sector). The white box outlines the AIA FOV. (B) displays the extracted annular region mapped onto polar coordinates, with the actual data extent marked by the white curve. Black lines indicate the directions used for measuring radial and lateral motions. (C) shows a stacked plot of intensity along the radial direction, with green markers highlighting intensity peaks and their corresponding distances from the CBF wavefront. The white lines represent the time interval during which the CBF is tracked within the AIA FOV. This figure is curated from (Kozarev et al. 2017).

2.4.1 Event Context

along shock-crossing magnetic field lines in the AIA FOV. In this section, I analyze a case study event in the low corona region and investigate plasma parameters

2.4 CBF Kinematics and Geometric Modeling: Case Study

The high-gated SPREEDAS-T array does similarly well across all metrics, as highlighted by Kozarev et al. (2022). Additionally, to ensure consistency in lateral kinematic measures, an averaging technique is applied to data from both lateral left and right flanks, as described in previous work by Kozarev et al. (2013) and Bryant et al. (2003). Majoring forward, the development of synthetic shock models (S2M) forms the next phase of the study, mentioned by Kozarev et al. (2022). These models, developed at a 24-second cadence, are constructed based on extrapolated radial and lateral kinematic results and incorporate major and minor axes of pharyngeal peristaltic waves. The shock surface is deformed from the onset of the CBF until it reaches 10 R_0 and then extended up to 30 R_0 utilizing results from the Magneot hydrodynamic model mentioned by Kozarev et al. (2022). The shock surface is deformed from the onset of the CBF until it reaches 10 R_0 and then extrapolated radially and laterally to generate comprehensive wavelets. The shock surface is deformed from the onset of the CBF until it reaches 10 R_0 and then extrapolated radially and laterally to generate comprehensive wavelets. This approach allows for a smooth transition of lateral kinematics from the onset of the CBF until it reaches 10 R_0 . The methodology for calculating the initial emission measure (DEM) during and before the event at each shock crossing and across shock structures. Notably, while the density jump within the AIA FOV typically remains below 1.2, regions beyond observational limits are assigned a value of 1.2, assuming the presence of weak shocks. To facilitate analysis, these synthetic shock model is segmented into distinct regions—the gap representing the shock nose, Zone 1, and Zone 2 representing the shock front—as explained by Kozarev et al. (2022). This segmentation aids in the examination of plasma parameter distributions across different sectors of the shock surface, as depicted in Figure 2.

The Solar Particle Radiation Environment Analysis and Forecasting—Acceleration and Scattering Transports (SPREADFAST) system, developed by Kozarev et al. (2022) and referred to as SPREADFAST throughout this discussion, operates as a physics-based prototype for forecasting SEP events within the framework of the CASH-IV framework. Built upon the SPREADFAST model, SPREADFAST integrates different methods to forecast SEP events at different timescales for different heliospheric regions.

2.3 Data Analysis and Methods

The were to be at 20% of the peak intensity. Furthermore, we applied mathematical techniques such as Levenberg–Marquardt least squares minimization (Makrilia et al. 2009) and bootstraping optimization (Fenton 1979) to the outer-order polynomials to fit the wave profiles, obtaining measurements of speeds, accelerations, intensities, and thicknesses in both radial and lateral directions.

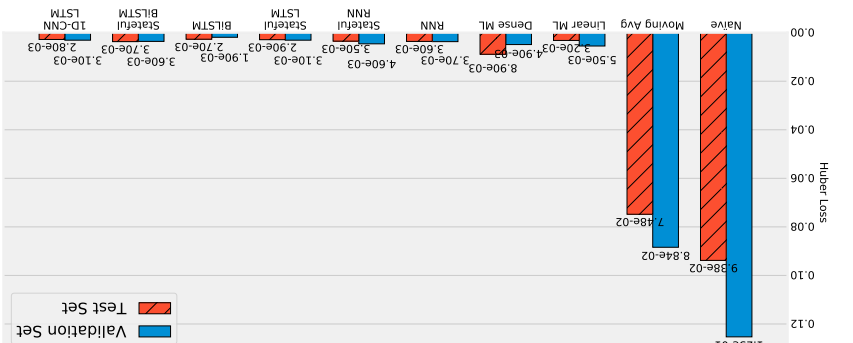
Figure 4: 3-day forecasts model predicted observations against short observations for 1-day, 2-day, and 3-day forecasts across energy channels. Correlation analysis on the time series sample test set showed high correlation across forecast windows. Correlation drops during solar cycle transitions.

Experiments with different batch sizes and optimizer learning rates as critical hyperparameters affect model performance (Geffert et al., 2016). Other architectural changes yield marginal improvements but via learning rate schedules instead.

average models. The BiLSTM model exhibited superior performance across validation and test sets. Three BiLSTM models, one per energy channel, were developed and trained to forecast SEP integral flux. Model performance was evaluated using Huber loss (Eq. 4), MAE, and learning rate adjustments

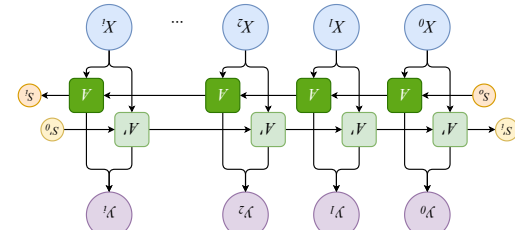
In Figure 4-3, ML-based methods showed similar performance, outperforming persistence and moving

4.2.3 Results and discussion



Multiclass evaluation metrics were utilized to assess model accuracy and performance, guiding further refinement.

Figure 4: The architecture of a single hidden BiLSTM layer. The figure is adopted from Olah (2015) and backward layers consists a single hidden BiLSTM layer. Both the forward and backward circles are the hidden states at the forward and backward layers, respectively. Below the forward green boxes are the activation units of the forward and backward layers, respectively. The orange and yellow boxes are the activation units of the forward and backward layers, respectively. The output values at multiple time steps labeled by (y_1, y_2, \dots, y_t) . The first green and light blue circles, on the other hand, are the input data values at multiple time steps. The purple circles, on the other hand, are x_1, x_2, \dots, x_t , are the input data values at the bottom layer, i.e., the input data values in the first time step, the time duration is denoted by (x_1, x_2, \dots, x_t) .



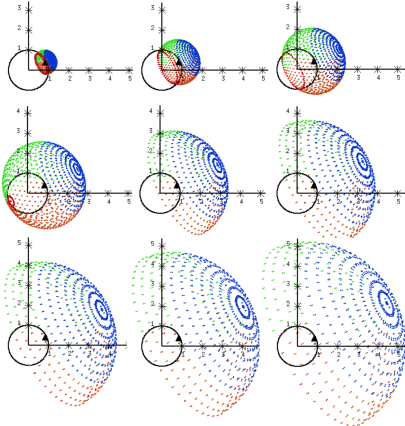


Figure 2.2: Synthetic shock model divided into three segments; the cap zone in blue and the flank zones in red and green.

partial-halo CME, with a linear speed of 745 km s^{-1} , a 2nd-order speed at $20 R_{\odot}$ of 776 km s^{-1} , and an acceleration of 3.3 m s^{-2} . The eruption was accompanied by a weak B8.1 solar flare and an eruptive filament observed by the SDO/AIA instrument. Additionally, a type II radio burst was associated with the eruption, observed by the Learmonth spectrogram. Proton fluxes near 1 AU showed an increase, and an SEP event was detected at Earth with onset time of 03:39 UT and a J_p of 0.0133 protons/(cm² s sr MeV) in the energy channel 17–22 MeV (Miteva et al. 2016, 2017). J_p is the peak proton intensity after subtracting the pre-event level.

2.4.2 Low Corona Part

To investigate the kinematics of the CBF event, I employed the CASHeW module within the SPReAd-FAST framework. The shock wave's asymmetrical evolution is detailed, along with its morphological changes over time. The average speeds and accelerations for the radial and lateral directions are provided (Fig. 2.4), along with a comparison of wave thickness between flanks. The shock surface is divided into segments for further analysis (Fig. 2.2). Table 2.2 provides a summary of the statistical results, and the results for the three segments are summarized in Table 2.3. Moreover, shock-crossing magnetic field lines during this event were investigated in (Kozarev et al. 2022), with key plasma parameters analyzed up to $10 R_{\odot}$. The aspect ratio of the coronal wave's geometry is discussed, along with changes in shock-field angle and magnetic field amplitude over time and radial distance.

2.4.3 Middle/Outer Corona Part

Complementary measurements from the SOHO/LASCO instrument⁵ expand the analysis of EUV waves' kinematics in the middle/outer corona. The height-time profile of the CME leading edge associated with the coronal wave is examined, employing fitting models of Gallagher et al. (2003) and Byrne et al. (2013) to analyze the data (Fig. 2.5). Insights into the wave's acceleration and speed variation over time and distance from the Sun are provided (Fig. 2.6).

2.5 Statistical Study

I conduct a thorough statistical analysis of coronal wave events observed in the AIA and LASCO FOVs, focusing on kinematic characteristics and plasma parameters.

⁵LASCO CME Catalog: https://cdaw.gsfc.nasa.gov/CME_list/

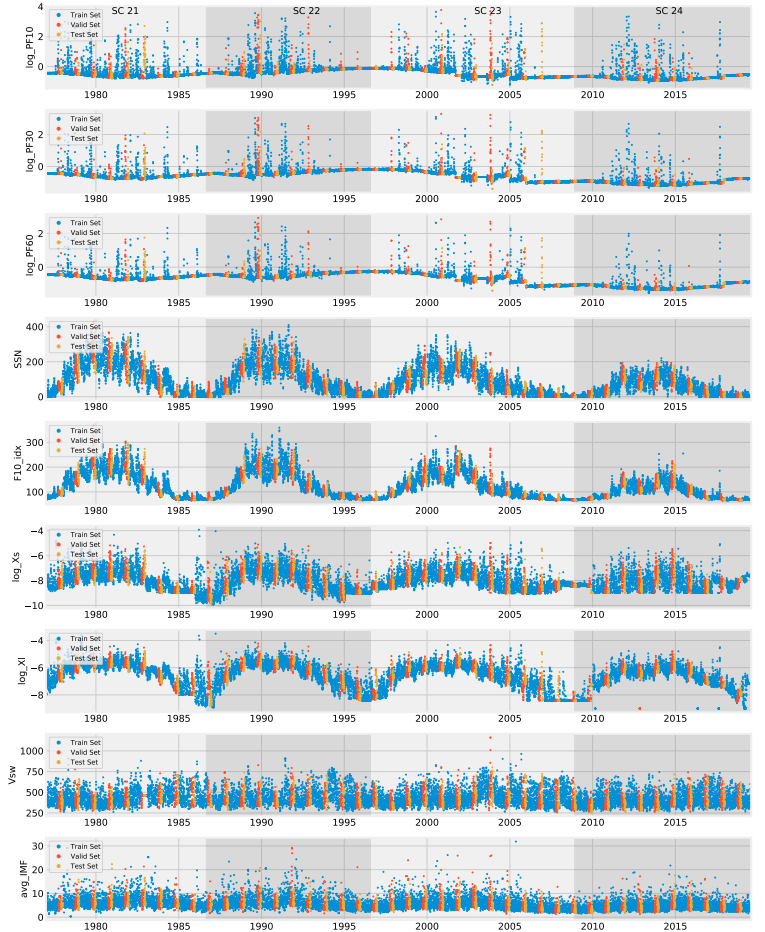
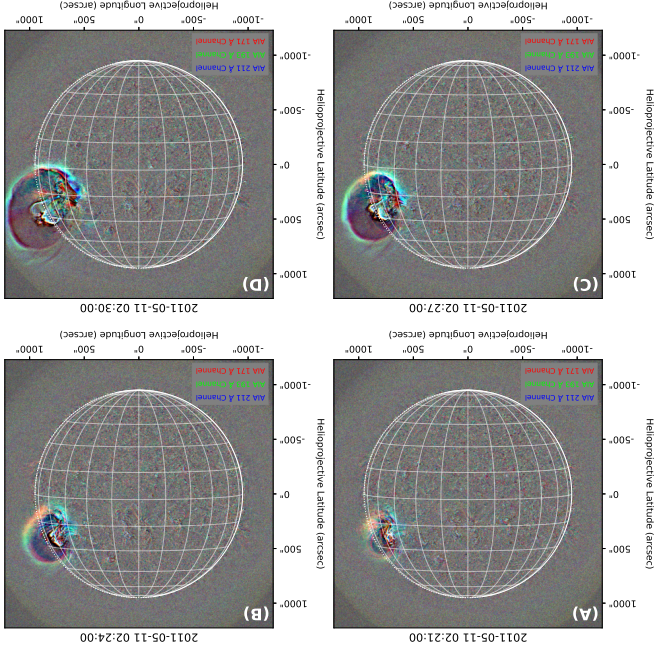


Figure 4.1: Data splitting for all input features, showing the training, validation, and testing sets. Daily data from 1976-12-25 00:00 to 2019-07-30 00:00. The gray shading labels the solar cycles from SC21 to SC24.

Parameter	Direction	Front	Peak	Back	$speed > km\cdot s^{-1}$	$accel. > m\cdot s^{-2}$	$intensity > DN$	$< thickness > R_{\odot}$
Lat. Left	218.46 ± 9.04	297.46 ± 54.45	293.94 ± 9.04					
Radial	427.46 ± 51.85	433.11 ± 82.86	400.81 ± 83.78					
Lat. Right	494.69 ± 0.00	509.25 ± 1.02	498.97 ± 9.21					
Lat. Left	-414.62 ± 227.23	-401.46 ± 104.62	-385.77 ± 227.23					
Radial	147.41 ± 1009.19	758.97 ± 127.65	485.88 ± 1365.80					
Lat. Right	-415.04 ± 0.00	-209.81 ± 22.32	-266.68 ± 250.80					
Lat. Left	250.60 ± 5.90	403.34 ± 133.30	489.04 ± 2.86					
Radial	0.07 ± 0.00	0.07 ± 0.00	0.07 ± 0.01					
Lat. Right	0.04 ± 0.01	0.04 ± 0.01	0.09 ± 0.00					

Table 2: Mean ratios and their standard deviation of the raw event count on May 11, 2011, in the SDO/AIA FOV.



This section outlines the data analysis methods employed in this study. It begins with an overview of model selection, followed by a detailed explanation of the Bi-directional Long Short-Term Memory (Bi-LSTM) architecture used to predict the near-Earth solar wind magnetic field and plasma parameters. The final section discusses the results obtained from the proposed model.

POWERS M. 511

This section outlines the data analysis methods employed in this study. It begins with an overview of model selection, followed by a detailed explanation of the Bi-directional Long Short-Term Memory (Bi-LSTM) architecture used to predict the near-Earth solar wind magnetic field and plasma parameters. The final section discusses the results obtained from the proposed model.

The Bi-ITSM Model

This section outlines the data analysis methods employed in this study. It begins with an overview of model selection, followed by a detailed explanation of the Bi-directional Long Short-Term Memory (Bi-LSTM) architecture used to predict the near-Earth solar wind magnetic field and plasma parameters. The final section discusses the results obtained from the proposed model.

RISSTM networks offer several advantages over traditional LSTM networks (Graves & Schmidhuber 2005; Hinton et al. 2020; Alahi et al. 2021). They excel in tasks like time-series forecasting, speech recognition, and language translation by capturing long-term dependencies in both directions (Wolmer et al. 2013; Graves & Jaitly 2014; Sutskever et al. 2014; Huang et al. 2018; Namarni et al. 2022). Additionally, they adapt well to variable-length sequences and handle noisy data. However, RISSTM networks are computationally intensive, require more parameters, and demand larger training datasets. The final dataset comprises 7 features, spanning from December 25th, 1976, to July 30th, 2019, totaling 15,583 samples. The model configuration includes 4 RISSTM layers with 64 neurons each and an output dense layer with 3 neurons representing the forecasting horizon. The total number of trainable parameters is 333,699.

To determine the most suitable model, I conducted comprehensive analyses, starting with baseline models like the native (persistence) model and moving-average model. Following this, I explored ML-based models using a windrowed dataset using a Multi-Input Multiple Output (MIMO) strategy, minimizing the imbalance of active and quiet days (Bennison et al., 2020). The Huber loss function was selected due to its robustness to outliers, crucial for our noisy data.

Model Selection

1 GOES SXR Database: <https://satdat.ngdc.noaa.gov/sem/>
2 OMNI Database: <https://omniweb.gsfc.nasa.gov>
3 Sunspot Number Dataset: <https://www.sci.gsfc.nasa.gov>

1 GOES SXR Database: <https://satdat.ngdc.noaa.gov/sem/>

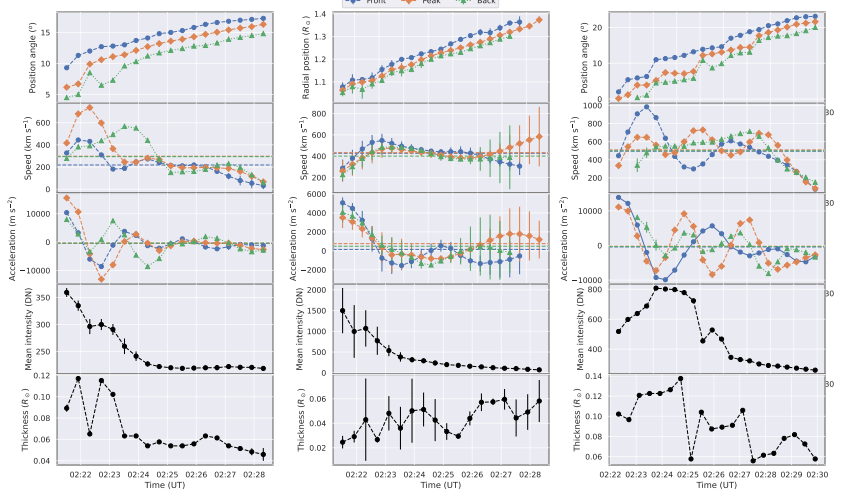


Figure 2.4: Time-series kinematics of the CBF parameters for the front, peak, and back positions in the AIA FOV, with measurement uncertainties shown as small bars over the data points. The horizontal lines in the speed and acceleration panels denote the mean speeds and accelerations for the wave front, peak, and back with respective colors. The left and right columns represent the lateral kinematic measurements in the left and right flanks of the wave, respectively. The middle column represent the kinematic measurements in the radial direction.

Table 2.3: Mean, median, and standard deviation of the shock parameters output, from the interaction of the S2M spheroid with the MAS MHD model results, for the shock's cap and flanks and for the whole shock surface, for the event on May 11, 2011.

Segment	Parameter	Statistics		
		Mean	Median	Stdv
All	V_{SHOCK} km s ⁻¹	577.77	578.39	72.79
	θ_{BN} °	70.06	0.63	44.83
	B_{MAG} G	0.046	0.038	0.070
	Density Jump	1.193	1.188	0.185
Cap	V_{SHOCK} km s ⁻¹	555.18	550.86	42.46
	θ_{BN} °	19.37	3.61	25.51
	B_{MAG} G	0.046	0.036	0.070
	Density Jump	1.193	1.188	0.015
Zone 1	V_{SHOCK} km s ⁻¹	613.69	609.32	59.42
	θ_{BN} °	6.46	0.21	50.92
	B_{MAG} G	0.045	0.045	0.066
	Density Jump	1.190	1.187	0.008
Zone 2	V_{SHOCK} km s ⁻¹	631.37	614.23	73.07
	θ_{BN} °	0.10	0.51	10.61
	B_{MAG} G	0.046	0.029	0.071
	Density Jump	1.194	1.188	0.016

Chapter 4

Modeling and Forecasting of Solar Energetic Protons

This chapter introduces a deep learning approach for forecasting the integral flux of energetic protons across three energy channels over three forecasting horizons.

4.1 Introduction

CMEs are pivotal in solar physics, attracting attention for their role in solar activity. Observations across various wavelengths provide insights into their dynamics (Vourlidas et al. 2003; Zhang & Dere 2006; Bein et al. 2011; Bastian et al. 2001; Veronig et al. 2010). Particularly, EUV observations, aided by instruments like AIA, have become crucial in capturing early CME stages (Lemen et al. 2012; Pesnell et al. 2012). CMEs can induce shock waves in the solar corona, observable as EUV waves or CBFs, crucial for SEP acceleration (Thompson et al. 1998; Long et al. 2011; Ontiveros & Vourlidas 2009; Gopalswamy & Yashiro 2011; Battarbee et al. 2013; Kozarev et al. 2013; Schwadron et al. 2014; Kong et al. 2017).

Previous research has focused on characterizing CME dynamics and their associated shocks, notably their relationship with CBFs (Kozarev et al. 2019). Extending this work, our study models CBF-related shock dynamics and particle acceleration up to $10 R_{\odot}$, integrating with a numerical particle transport model, marking a significant advancement in Sun-to-Earth physics-based modeling (Kozarev et al. 2022).

SEP production by coronal shocks throughout the inner heliosphere has garnered attention. CMEs, particularly in their early stages, play a major role in SEP acceleration (Reames 1999; Ontiveros & Vourlidas 2009; Gopalswamy & Yashiro 2011; Battarbee et al. 2013; Kozarev et al. 2013; Schwadron et al. 2014; Kong et al. 2017). Our study extends modeling of CBF-related shock dynamics and particle acceleration, marking the first validated Sun-to-Earth physics-based modeling for SEP acceleration and transport (Kozarev et al. 2022).

Various models exist for SEP forecasting (Whitman et al. 2023), including physics-based, empirical, and Machine Learning (ML) based models. Notably, the PROSPER model provides probabilistic predictions for multiple energy channels (Papaioannou et al. 2022), while ML approaches offer promising avenues for accurate and rapid forecasting (Lavasa et al. 2021; Kasapis et al. 2022). Despite advancements, forecasting SEP fluxes remains challenging, emphasizing the need for dependable forecasting systems. In upcoming sections, we address challenges in modeling SEP fluxes, particularly focusing on imbalanced datasets and low-resolution data. Our study builds upon previous work on CBF kinematics discussed in Chapter 2 and presents advanced deep learning models for forecasting daily integral flux of SEP, offering insights into space radiation profiles.

4.2 Solar Proton Flux Forecasting with Deep Learning Models

4.2.1 Data Preparation

This section outlines the selection of input physical quantities, their sources, and the forecasting outputs. Two categories of input features are considered: remote signatures and in-situ measurements. Remote signatures include the F10.7 index, long-wavelength (X_L), and short-wavelength (X_S) x-ray fluxes, ob-

Figure 2.5: Top panel – Height-time profile compiled from AIA and LASCO measurements for the event occurred on May 11, 2011, fitted with two CMIE kinematics models from the photosphere up to $17 R_\odot$. Middle panel – Difference between the fitting and the real observations. Bottom panel – Relative residuals in %.

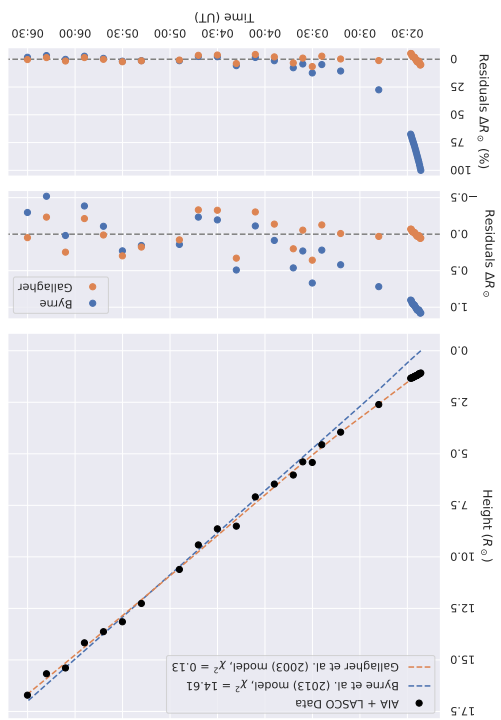
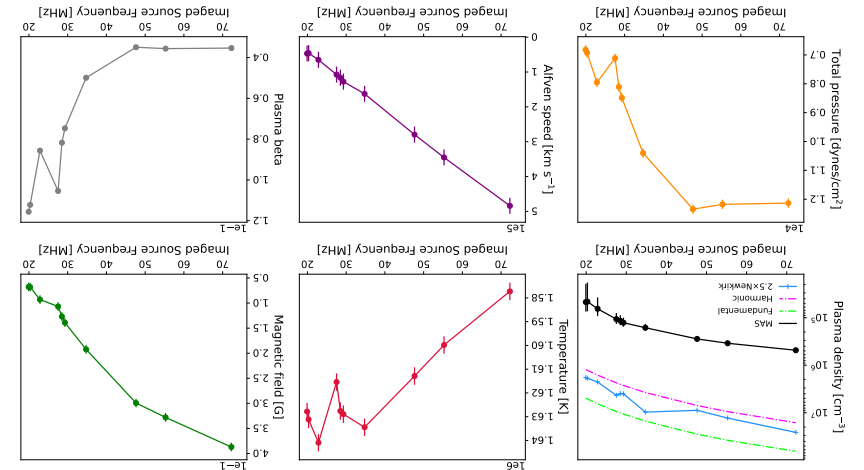


Figure 3.9: Coronal plasma parameters sampled from the 2D maps by the source centroids. The top panel shows (from left to right) the plasma density profiles from the MAS model, $2.5 \times$ Newkirk model, and the theoretical densities under the kinematical and harmonic assumptions, plasma temperature, and magnetic field. The bottom panel shows the plasma beta to right, the total plasma dynamic pressure, Alfvén speed, and plasma beta. The x-axis is inverted to demonstrate a progression of increasing radial distance from the Sun as the observer moves towards the right.



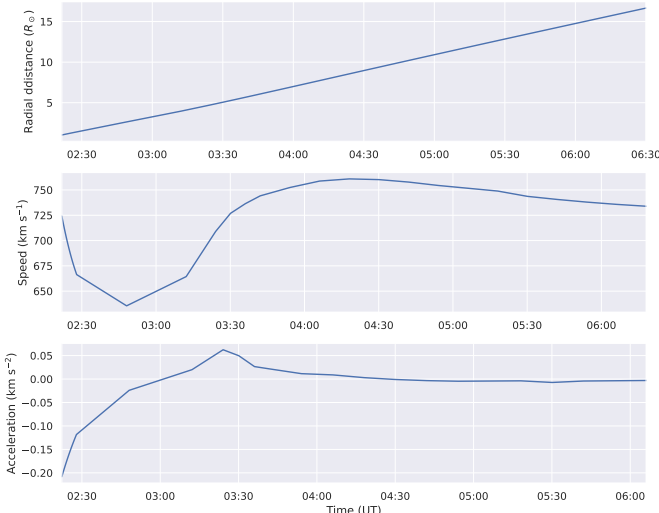


Figure 2.6: Extrapolated radial kinematics for the event occurred on May 11, 2011, based on the ballistic model of Gallagher et al. (2003) up to $17 R_{\odot}$.

Table 2.4 summarizes statistical parameters related to shock characteristics, such as wave speed, intensity, and thickness in the AIA FOV. Analysis reveals higher speeds, accelerations, lower mean intensities, and thickness in the radial direction compared to the lateral direction, suggesting early elongation of waves near the Sun. Figure 2.7 illustrates EUV waves' kinematics evolution in the AIA FOV, showing parameter distributions as a function of distance for shock speed, acceleration, wave intensity, and thickness in radial and lateral directions. Speed and intensity decline with distance due to momentum loss and decreasing plasma densities. All dynamic spectra for individual events are accessible on the SPREAdFAST catalog webpage⁶.

Table 2.4: Statistics of the EUV wave kinematics in the SDO/AIA FOV for the 26 events. LL and LR refer to the lateral left and right flanks, respectively. Rad refer to the radial front direction.

Aspect ratio	Speed (km s^{-1})			Accel. (km s^{-2})			Intensity (DN)			Thickness (R_{\odot})			
	LL	Rad	LR	LL	Rad	LR	LL	Rad	LR	LL	Rad	LR	
Max	2.00	1574.81	2053.73	983.58	28.19	81.01	13.89	1348.87	2431.95	1498.45	9.600	0.185	6.100
Min	0.84	2.11	40.30	2.30	-35.24	-81.01	-9.89	0.53	0.17	150.30	0.027	0.018	0.022
Mean	1.87	316.17	413.60	264.50	-0.15	0.98	0.13	438.99	681.46	442.46	0.715	0.059	0.231
Median	2.00	284.77	349.32	216.32	0.03	0.37	0.11	337.96	425.23	389.06	0.102	0.055	0.076
Stdv.	0.33	261.01	336.11	191.13	5.53	11.08	2.05	292.26	592.78	227.10	1.721	0.030	0.776

Histograms in Figure 2.8 depict correlations between shock-field angle "THBN", coronal magnetic field "BMAG", plasma density "DENSITY" Alfvén speed "VA", shock speed, and shock density jump "SHOCKJUMP". Moderate positive correlations exist between magnetic field and density, and between magnetic field and Alfvén speed, suggesting common underlying physical processes. A negative correlation between magnetic field and shock density jump implies stronger magnetic fields associate with smaller density jumps across shock surfaces, possibly due to magnetic field pressure resisting plasma compression or faster Alfvén waves mitigating density jumps. Further exploration is warranted to establish definitive connections and parameterize shock density jumps.

⁶SPREAdFAST Catalog: <https://spreadfast.astro.bas.bg/catalog/>

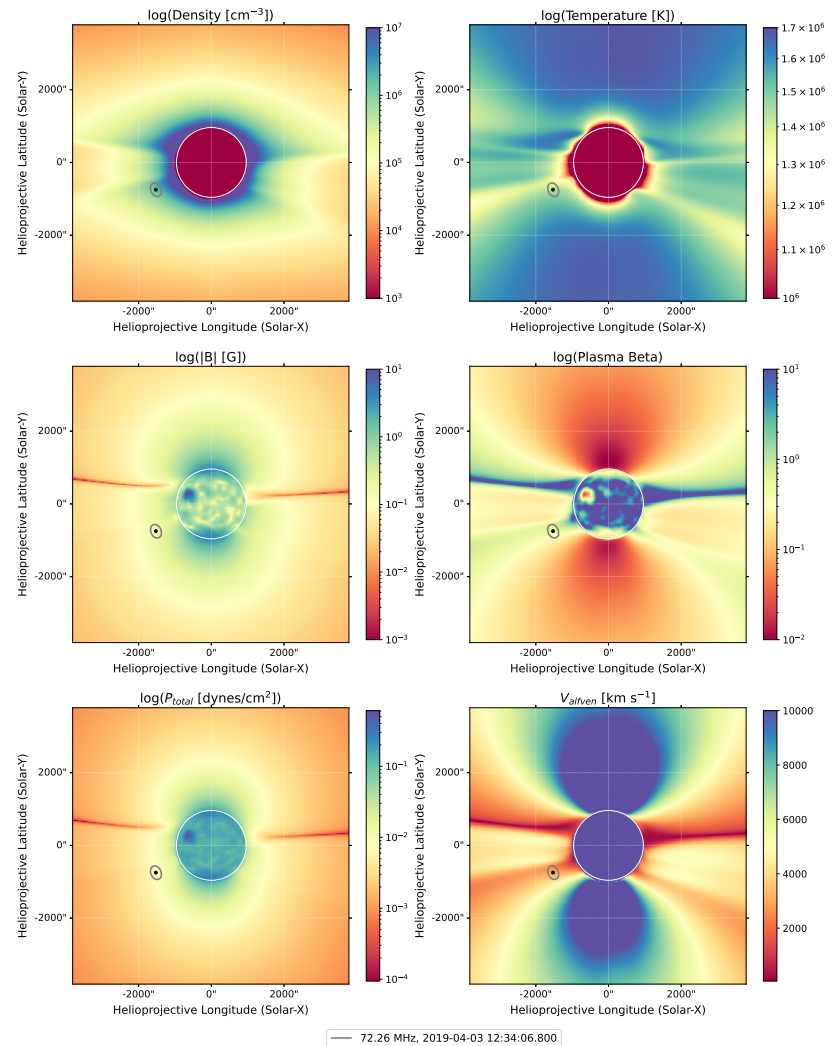


Figure 3.8: Synthesized maps of plasma parameters obtained using the FORWARD toolset, with the 70%-contour of radio emission of the sixth burst at the first timestamp (12:34:06.8 UT) at the frequency of 72.26 MHz depicted on top of the 2D POS cuts. The left column represents, from top to bottom, plasma density, magnetic field, and the total plasma dynamic pressure. The right column represents, from top to bottom, the temperature, plasma beta, and the Alfvén speed.

Figure 27: Dynamic waveforms binematics in the AIA FOV. The panels from the top to the bottom left are the wave speeds, accelerations, mean intensities, and thicknesses. The central left Bank, the central column is for the radial direction, and the right column is for the lateral directions. The bottom are the wave speeds, accelerations, mean intensities, and thicknesses. The left column is for the radial direction, and the right column is for the lateral directions. The right Bank, the central column is for the radial direction, and the right column is for the lateral directions.

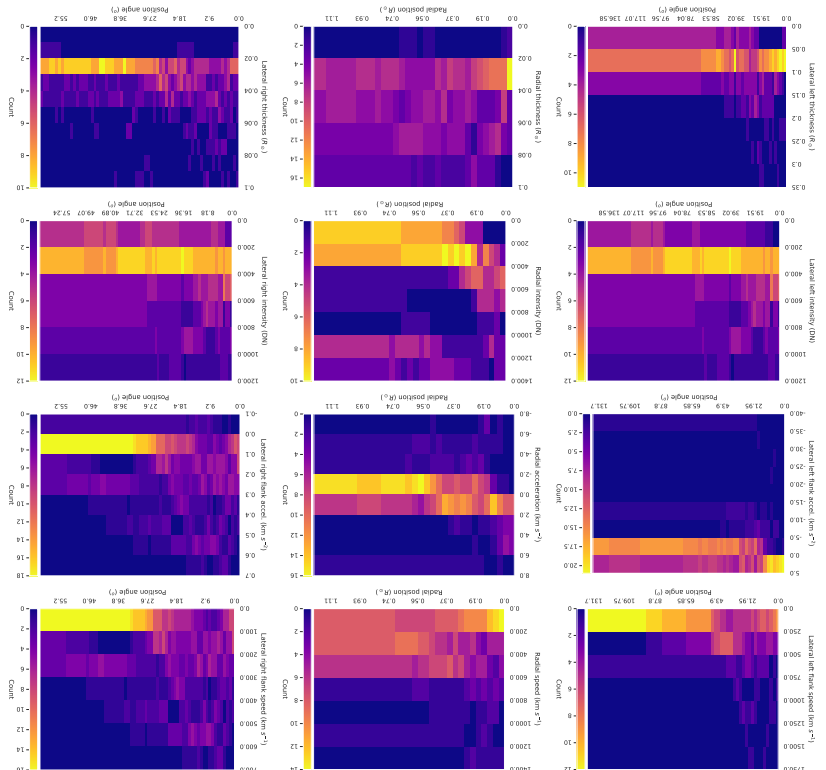
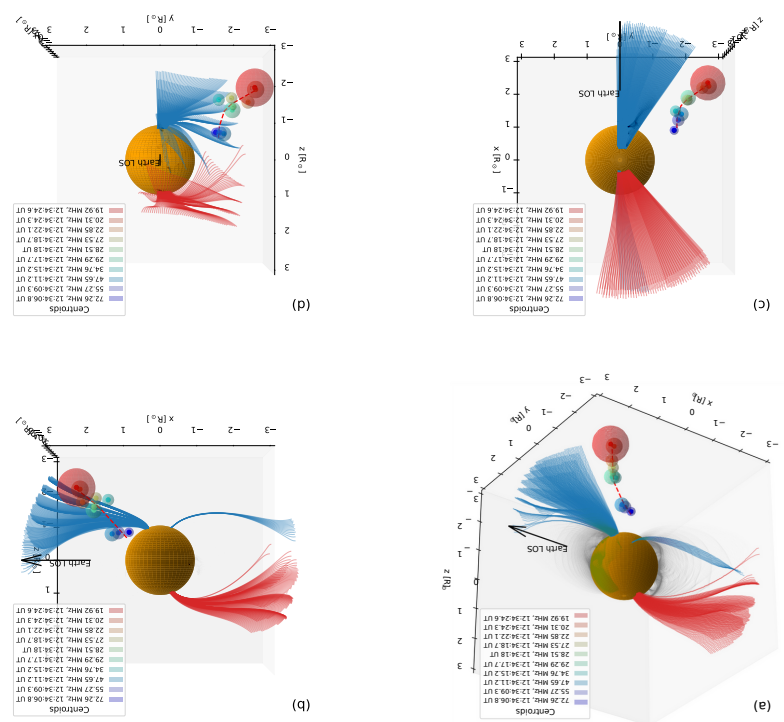


Figure 37: Different viewing angles for the deprojection of the radio sources of the sixth burst using the 2.5×Newmark electron-density model on the PFSS solution. The black arrow points toward the Earth's LOS, The yz plane is the POS as seen from the Earth. The red dashed line is a spline curve fit for the LOS sources, correspondingly. The red, black, and blue curves are the open northern, closed, and open southern field lines, respectively. The opacity of the field lines is decreased for better visualization.



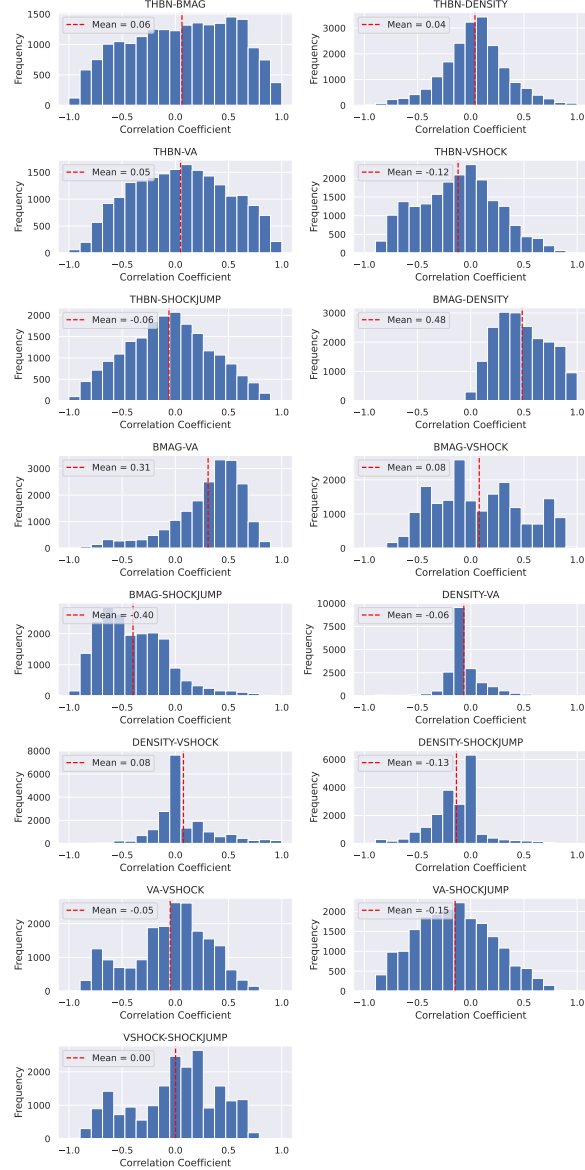


Figure 2.8: Histograms of along-field-lines model plasma parameters in the solar corona for all the 26 events. The vertical dashed red lines are the mean values.

the southern hemisphere and open field lines from the southern coronal hole. However, limitations exist due to outdated magnetic data for AR12738.

The potential origins of type III radio emissions include closed-field lines structures, electron beams from open-field active regions, or from corona acceleration due to magnetic field expansion in active regions. Furthermore, an inverse relationship between imaging quality and solar radio emission brightness was noted, attributed to calibration solution inaccuracies caused by solar emission leakage into calibrator beam side lobes.

3.4.3 Plasma Diagnostics and Magnetic Field Analysis

The alignment of radio sources (Fig. 3.7) with a streamer-like structure near the equator indicates elevated plasma beta, reduced coronal temperature, and diminished Alfvén speed. However, the coronal plasma density appeared homogeneous with no prominent structures due to model resolution limitations. Radio sources for all bursts were found in the same quadrant from Earth's perspective, confined between the equatorial sheet and the southern coronal hole and moving along that boundary.

Variability of coronal plasma quantities at radio sources' centroids was observed (Fig. 3.9), with coronal temperature increasing with radial distance. Additionally, the behavior of coronal magnetic field, plasma total dynamic pressure, and Alfvén speed decreased over distance. Plasma beta parameter sharply increased around 40 MHz, suggesting dominance of plasma pressure over magnetic pressure at that distance from the Sun.

Comparison of density profiles (Fig. 3.9) indicated significant differences between MAS and FORWARD modeling results compared to the $2.5 \times$ Newkirk density model and theoretical expectations. The discrepancy, even after accounting for enhancement factors, suggests possible scattering effects or stealth CMEs affecting density observations, highlighting limitations in current modeling and suggesting the need for additional physics to characterize density distribution accurately.

3.5 Summary and conclusions

In this study (Nedal et al. 2023b), a series of 16 type III bursts observed on April 3, 2019, during the PSP's near-Sun encounter, were analyzed using PSP/FIELDS and LOFAR. These bursts, spanning nearly 20 minutes, occurred amidst relative solar quietness with a dominant active region on the solar disk. A semi-automated pipeline aligned PSP and LOFAR observations, facilitating analysis of burst characteristics like frequency drift and electron beam speeds, suggesting their interrelation.

Interferometric imaging revealed a single source for these bursts in the solar corona's southeast limb. Various potential origins for the bursts were discussed, including impulsive events (Ishikawa et al. 2017; Che 2018; Chhabra et al. 2021), plasma upflows (Harra et al. 2021), and magnetic reconnection (Gopalswamy et al. 2022a). Magnetic extrapolation indicated no open potential field lines to active regions AR12737 or AR12738, consistent with prior findings.

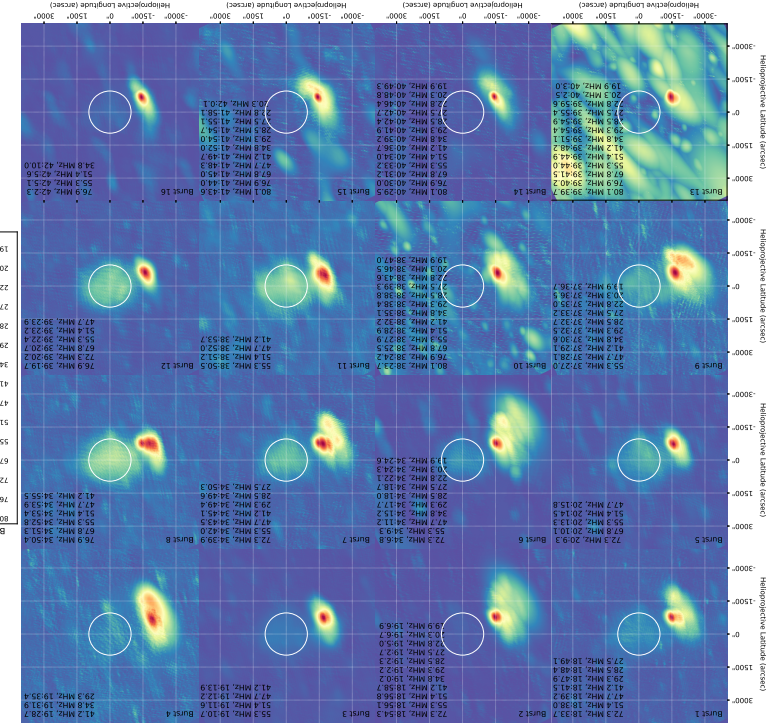
Integration of burst source location with magnetic modeling suggested discrepancies, possibly due to scattering effects. Scattering and propagation effects were found significant, impacting burst location determination. Future investigations, including the TDoA technique and Solar Orbiter observations, were proposed.

The study highlighted LOFAR's efficacy in characterizing solar eruptive events and quiet periods, with implications for space weather monitoring. Future work aims to automate burst analysis and investigate their relation to solar surface activity. Additionally, analysis using LOFAR imaging and MAS modeling indicated discrepancies between observed and modeled burst trajectories, emphasizing the need for model refinements. Overall, this study underscores the importance of considering scattering effects and refining models to enhance understanding of solar radio emissions' propagation in the corona (Kontar et al. 2019, 2023; Chen et al. 2023).

I conducted a study characterizing 26 historical CME-driven CBFs in the low solar corona, observed with the AIA instrument onboard the SDO spacecraft. Utilizing the SPReDFAST framework, we integrated physics-based and data-driven models to estimate coronal magnetic field lines, shock wave dynamics, energetic particle acceleration, and SEPP propagation. The analysis is based on AIA base-difference images to generate particle-acceleration and SEPP spectra characteristics, and thickness, and thickness, LASCO measurements facilitated time-dependent 3D geometric models of wavefronts and informed plasma diagnostics through MHD and DEM models. Various time-dependent and distance-dependent kinematic parameters were used to fit geometric surface models for each time step, shock kinematic measurements were used to fit geometric surface models for each time step, capturing shock characteristics accurately. Parameterized relationships between plasma parameters were explored to identify connections and interdependences. The midplane contributes to understanding shock kinematics and plasma parameters. Future investigations will focus on SEPP acceleration near the Sun and transport of coronal and interplanetary particles, refining shock and coronal parameter characterization methods for enhanced accuracy and reliability.

2.6 Conclusions

Figure 3: Persistence imaging for the 16 type III bursts detected in the LOFAR dynamic spectrum. The label shows the observation frequency in MHz and times in minutes:seconds from 12:00:00 UT. The label shows the observation frequency in MHz and times in minutes:seconds from 12:00:00 UT. Here, the color coding is not absolute, but rather each panel has its own color code.



Chapter 3

Solar Radio Observations

Integrating Data for Coronal Diagnostics

In this chapter, I focus on multi-wavelength observations of solar type III radio bursts and modeling studies of plasma parameters and coronal magnetic fields to understand solar radio emission mechanisms during quiet times and coronal conditions influencing burst propagation. Initially, I introduce type III radio bursts and detail the data used, followed by output presentation and interpretation.

3.1 Introduction

Type III radio bursts result from energetic electron beams injected into the solar corona, propagating along IMF lines Ergun et al. (1998); Pick (2006); Reid (2020). These beams trigger plasma waves, transformed into radio emission at local plasma frequency or its harmonics Melrose (2017). They manifest as intense emissions drifting in frequency over seconds to minutes, detectable across a wide frequency range Wild & McCready (1950); Lecacheux et al. (1989); Bonnin et al. (2008), offering insight into solar active phenomena Reid & Ratcliffe (2014); Kontar et al. (2017).

Electron beams persist well beyond 1 AU, providing in situ insights into burst and ambient heliospheric conditions, including electron density, beam speed, and Langmuir wave detection Dulk et al. (1985); Boudjada et al. (2020); Gurnett & Anderson (1976, 1977); Reid & Ratcliffe (2014). Combining ground-based and space-borne observations is crucial for comprehensive analysis.

This work studies type III bursts on April 3, 2019, using data from LOFAR van Haarlem et al. (2013) and PSP Fox et al. (2016), integrating PFSS and MAS models Altschuler & Newkirk (1969); Schatten et al. (1969); Mikić et al. (1999). LOFAR imaging provides burst source localization, expanding knowledge of electron beam triggers and coronal conditions. Understanding these aspects is crucial for comprehending solar energetic particles, solar wind, and their effects on near-Earth space.

Previous studies have investigated type III burst mechanisms Chen et al. (2013); Bonnin et al. (2008); Reiner et al. (2009); Saint-Hilaire et al. (2012); Morosan & Gallagher (2017); Pulupa et al. (2020); Krupar et al. (2020); Cattell et al. (2021); Harra et al. (2021); Badman et al. (2022). Modern instruments like LOFAR and PSP offer enhanced sensitivity, yet challenges remain, including electron acceleration mechanisms and discrepancies between observations and models.

The chapter is structured as follows: Section 3.2 describes LOFAR and PSP observations of type III bursts; Section 3.3 explains data analysis and modeling techniques; Section 3.4 presents analysis results, investigating physical mechanisms and comparing with solar corona models; and Section 3.5 summarizes findings and discusses implications.

3.2 Observations

Several studies have investigated solar radio emissions during the PSP's second encounter in late 2019 Krupar et al. (2020); Pulupa et al. (2020); Cattell et al. (2021); Harra et al. (2021); Badman et al. (2022). This study focuses on type III radio bursts occurring on April 3, 2019, between approximately 12:10 and 12:50 UT, coinciding with active regions AR12737 and AR12738. AR12737, on the near side of the Sun, exhibited a β magnetic configuration with eight sunspots Hale et al. (1919), while detailed observations of AR12738 were unattainable due to its far-side position.

type III sources was performed to estimate their 3D positions relative to Earth's line of sight (LOS) (Fig. 3.7). Axes translations between LOFAR images and 3D space were accounted for. Detailed explanations and equations are provided in Appendices ?? and ??.

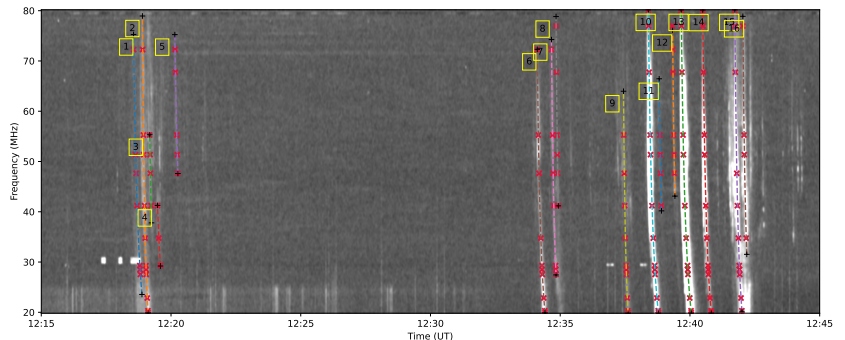


Figure 3.5: Automatic detection of type III bursts observed by LOFAR. The red symbols along the fit lines are the (f, t) coordinates of the image snapshots shown in Figure 3.6.

3.3.2 Modeling

To analyze the coronal plasma environment during the events, I utilized standard coronal solutions from MHD simulations by Predictive Science Inc. (PSI) based on the MAS code (Mikić et al. 1999). The PSI MAS coronal solution for April 3, 2019, at 12:00 UT was obtained from the PSI data archive. Initially, I determined the angle between the burst's radial vector and the line of sight (LOS), as well as the complement angle representing the separation between the radial vector and the Earth's perspective. Using the complement angle, I derived the Carrington longitude to extract a longitudinal segment from the MAS datacube, treating it as if it were in the plane of the sky (POS). Longitudinal slices were extracted using the psipy python package. The FORWARD model, responsible for generating synthetic coronal maps, was then applied to the selected data slice. In Figure 3.8, the first radio contour of the sixth type III burst is overlaid on 2D maps of plasma parameters. These parameters include plasma density, temperature, magnetic field strength, plasma beta parameter, total plasma pressure, and Alfvén speed. Estimates of local plasma conditions at the centroids' coordinates of type III sources for each frequency band are illustrated in Figure 3.9 for the sixth type III burst.

3.4 Results and discussion

3.4.1 Type III Radio Burst Detection and Characterization

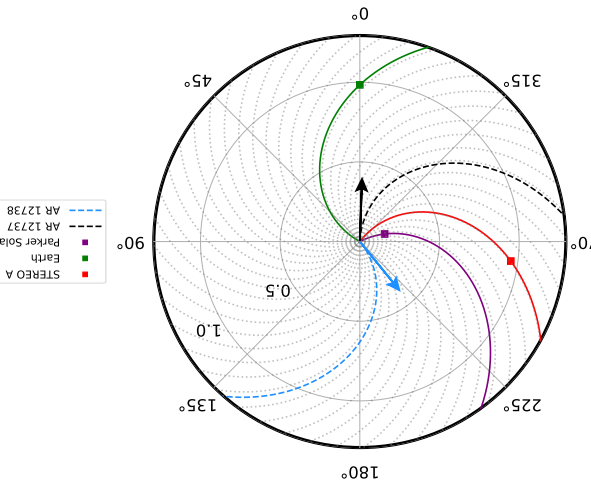
Radio waves arrived at STEREO one minute before reaching Wind (Fig. 3.1). However, due to the close proximity to the Sun, the difference in arrival times is within the resolution of the observations, making it inconclusive which spacecraft detected the emission first.

The combined dynamic spectrum from LOFAR and PSP (Fig. 3.4) showed limitations in detecting type III bursts compared to LOFAR alone, possibly due to frequency drift and dispersion challenges. Nine bursts were captured from the combined spectrum, while 16 were traced in LOFAR alone (Table 3.1).

3.4.2 Imaging of Radio Emission Sources

Persistence imaging of the 16 type III bursts from LOFAR (Fig. 3.6) suggested a common origin in the south-east quadrant of the solar disk, despite the absence of an active region at that precise location. A 3D projection of radio source contours onto the coronal magnetic field (Fig. 3.7) revealed a south-eastward propagation relative to Earth's perspective. The radio sources aligned with closed field lines in

Figure 3-2: Top view of the spectrum positions in the elliptical plane at 12:15 UT on April 3, 2019, with the Sun-Earth line as the reference point for longitude. The Earth's location is represented by the center position of LOFAR, WIND/WAVES, and GOES-15/XRS instruments. The spectrum野外 were centered back to the Sun by a 400 m/s preference Parker Spiral, the black arrow represents the longitude of AR12737 and the blue arrow represents the longitude of AR12738. The gray dotted lines are the background Parker spiral field lines. The black dashed spiral is connected to the AR12738. The figure is generated using the Solar Magnetic Connection Hubs (Solar-MACH) tool (Gissler et al. 2023).



The vertical red dashed line denotes the start time of the burst. The bottom-left is from the STEREO/SWAVES instrument, and the top-right is from the PPS/FIELDS instrument, the top-left panel is from the LOFAR/LBA instrument, and the top-right panel is from the Wind/WAVES instrument.

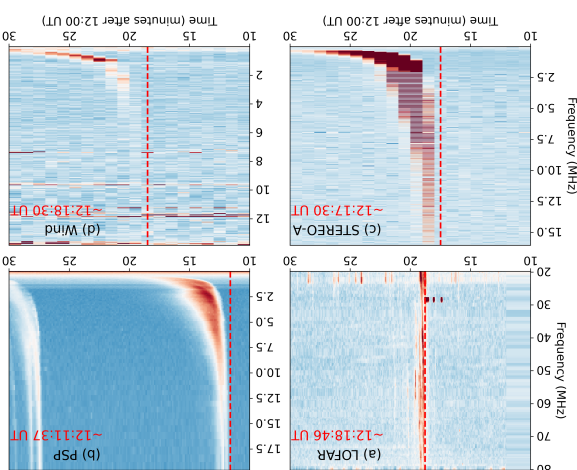
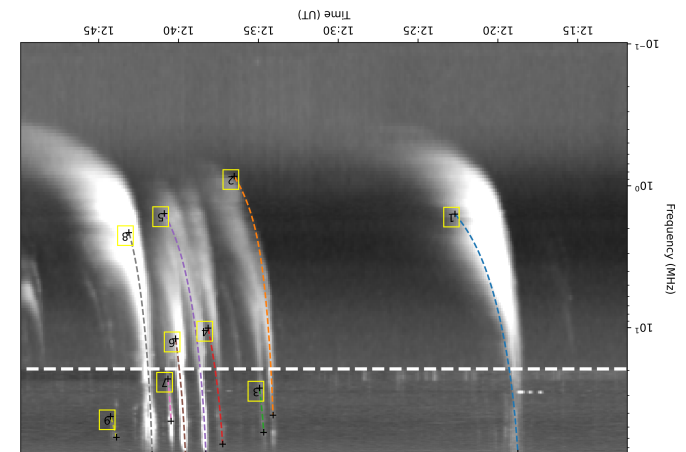


Table 3.1: Characteristics of the type III bursts detected via the automatic algorithm from the combined

ID	Burst Start Time	End Time	Start Frequency	End Frequency	Frequency Drift	Burst Speed
1	12:18:45	12:22:42	76.4M	15.7T	0.982	0.044
2	12:34:05	12:38:31	41.2A	0.86	0.241	0.119
3	12:41:04	12:43:46	54.4M	26.5A	3.992	0.046
4	12:37:14	12:40:09	66.0B	10.02	4.006	0.046
5	12:38:17	12:40:54	76.92	1.57	0.77	0.066
6	12:23:34	12:24:01	78.86	11.93	3.129	0.062
7	12:40:28	12:40:40	45.3A	22.9	3.21	0.067
8	12:21:39	12:23:06	78.21	2.13	1.555	0.093
9	12:24:35	12:24:45	59.07	42.13	2.421	0.013

Figure 34: Automatic detection of type III radio bursts from the combined radio dynamic spectrum of LOFAR and the PSD frequency range (bottom).



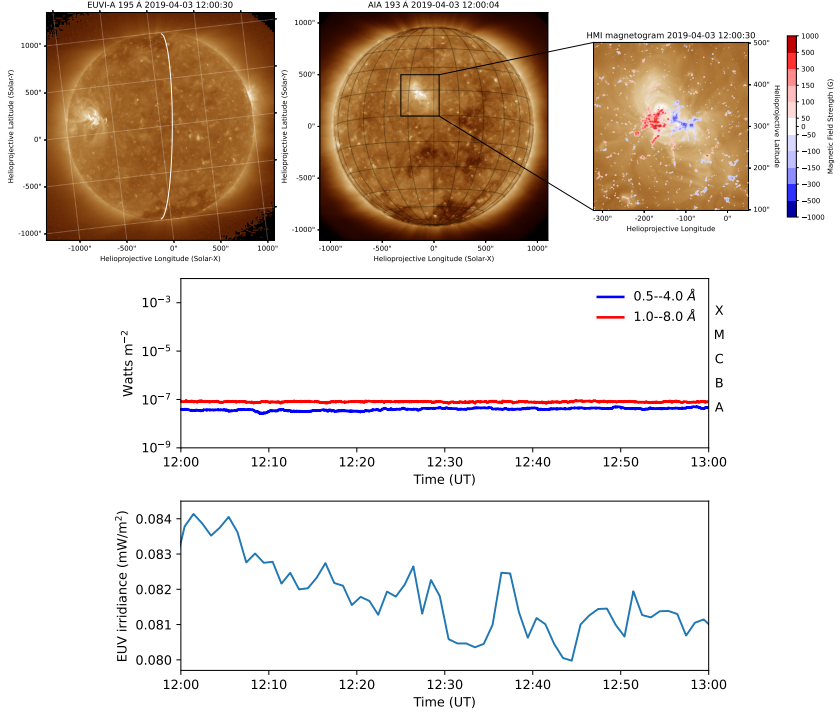


Figure 3.3: Exploring the X-ray and EUV emissions from the Sun. The top panel showcases a cutout region of the SDO/AIA 193 Å image of the solar disk along with the STEREO-A EUVI 195 Å point of view. The white curve is the limb of the solar disk as seen by AIA from the right side. The red and blue colors are the contours of the line-of-sight magnetogram from the SDO/HMI instrument. The levels are (50, 100, 150, 300, 500, 1000) Gauss. The middle panel shows the X-ray flux from the GOES-14 spacecraft shows minimum activity. The bottom panel shows the time series of the ESP Quad band from the SDO/EVE instrument, which shows the solar irradiance in the EUV band.

Intense type III radio bursts were observed by four instruments (Wind/WAVES, PSP/FIELDS, STEREO-A/SWAVES, and LOFAR/LBA) during a regular survey. Figure 3.1 displays the first type III burst observed by these instruments, with the start time determined using the second derivative of the light curve at specific frequency channels. The relative orientations of the instruments with respect to Earth are shown in Figure 3.2, with PSP and STEREO spacecraft almost aligned with the Sun. The solar disk appeared quiet, with no X-ray or EUV transient emissions during the study period, confirmed by GOES-15/XRS and SDO/EVE observations. Despite this, the sensitive LOFAR telescope detected bursts close to noon, corroborated by PSP data.

Localized regions of relatively higher intensity, likely small-scale coronal brightening spots or campfires, were observed in EUVI and AIA images Young et al. (2018); Madjarska (2019); Berghmans et al. (2021). Subsequent subsections introduce the PSP and LOFAR instruments and their observations of the radio bursts.

3.2.1 PSP Observations

Parker Solar Probe (PSP) is a spacecraft launched in 2018 to study solar corona and solar wind (Fox et al. 2016). I utilized level-2 data from the FIELDS instrument suite (Bale et al. 2016; Pulupa et al. 2017), available in CDF format on the PSP FIELDS data products website¹. Data values were converted from V^2/Hz to dB units using a threshold of $10^{-16} \text{ V}^2/\text{Hz}$ for radio burst detection (Pulupa et al. 2020). High- and Low-Frequency Receiver data were combined into a single dynamic spectrum covering 10.5 kHz to 19.2 MHz, with noise minimized through subtraction of mean intensity values.

3.2.2 LOFAR Observations

The Low Frequency ARray (LOFAR) telescope (van Haarlem et al. 2013) observes the Sun at frequencies between 10 and 240 MHz. Dynamic spectrum data from the Low-Band Antenna (LBA) were obtained from the LOFAR long-term archive². Background subtraction and Gaussian smoothing were applied to clean the spectrum. PSP and LOFAR spectra were combined, considering the travel time difference of radio signals from the Sun to each instrument. LOFAR data were down-sampled to match PSP's 7-second cadence. The resulting combined spectrum is shown in Figure 3.4. LOFAR's LBA frequency ranges between 19.82 and 80.16 MHz, while PSP's cover 10.55 kHz to 19.17 MHz.

To automatically detect type III radio bursts in the combined dynamic spectrum, I applied the algorithm proposed by Zhang et al. (2018), which employs probabilistic Hough transformation to detect vertical bright edges within a specified deviation angle from the vertical direction.

3.3 Methods

3.3.1 Imaging of Radio Sources

I developed an automated pipeline to preprocess and calibrate LOFAR interferometric data for solar radio imaging (Zhang et al. 2022a). Burst detection was performed using the algorithm by Zhang et al. (2018) on combined LOFAR and PSP dynamic spectra (Fig. 3.4). The Parker electron-density model (Parker 1960) was employed to map bursts to radial distances, with least-squares fitting used to derive frequency drifts and electron beam speeds.

Subsequently, burst detection was repeated on LOFAR dynamic spectra alone (Fig. 3.5) to identify (f, t) pairs for each burst. Snapshot frequencies were selected for interferometric imaging, calibrated using Tau-A observations. The WSClean algorithm (Offringa et al. 2014) was applied to obtain cleaned images of radio sources at the chosen frequencies.

Persistence imaging was employed to enhance image clarity and information content (Thompson & Young 2016). This method compares pixel values across a time-ordered series of images, retaining the brightest values to create a persistent display.

To determine type III source locations in 3D space, LOFAR observations were combined with modeling. Grids of footpoints were constructed on GONG magnetogram data around active regions AR12737 and AR12738. Pfsspy package (Stansby et al. 2020) traced coronal magnetic field lines, aiding in estimating source radii and 3D positions. Radial distances of sources from the Sun were determined assuming harmonic emission, considering Newkirk electron-density models (Newkirk 1961, 1967). Deprojection of

¹PSP FIELDS data products: <http://research.ssl.berkeley.edu/data/psp/data/sci/fields/>

²LOFAR LTA: <https://lta.lofar.eu/>